communications biology

A Nature Portfolio journal

Article

https://doi.org/10.1038/s42003-025-09248-5

Engineering CCR2/IFN-γ overexpression in enucleated mesenchymal stem cells enhances therapy for rheumatoid arthritis

Yue Sui[1,4], Zixi Pu[1,2,4], Naixue Yang[1,4], Yifei Luo[1,2], Yalian Sa[3], Qi Qi[1], Li Tan[1], Yaping Yan[1] ✉ & Wei Si[1,2] ✉

Mesenchymal stem cells (MSCs) offer a promising therapy for rheumatoid arthritis (RA). However, their therapeutic potential is hindered by initial trapping in lung capillaries, which may reduce efficacy and increase risks of complications, such as unwanted differentiation and malignancy. Additionally, engineering MSCs to enhance therapeutic effects introduces further safety concerns and regulatory challenges for clinical approval. In this study, we generated enucleated human umbilical cord-derived MSCs overexpressing CCR2 and IFN-γ (En-MSCs$^{C/I}$), which retained essential organelles and exhibited immune regulatory, paracrine, and homing capabilities. Intravenous administration of either MSCs or En-MSCs$^{C/I}$ alleviated synovitis in a male rat model of RA by modulating immune and inflammatory processes of fibroblast-like synoviocytes and myeloid cells, as revealed by single-cell RNA sequencing analysis. En-MSCs$^{C/I}$ promoted the secretion of factors such as SEMA3E, potentially contributing to synovitis amelioration and cartilage regeneration. Compared to MSCs, En-MSCs$^{C/I}$ demonstrated superior migration to injured joints and unique regulatory signature for cartilage regeneration. Our study suggests that En-MSCs$^{C/I}$ may offer enhanced therapeutic effects for RA-related cartilage damage while maintaining favorable safety profiles.

Rheumatoid arthritis (RA), which affects approximately 1% of the global population, is a common systemic autoimmune disease triggered by both genetic and environmental factors[1,2]. It is characterized by chronic joint inflammation resulting in pain, stiffness, and joint swelling. Aggressive synovitis results in cartilage destruction, bone erosion and joint deformity, and involvement of vital organs[3]. Therefore, effective treatment for RA is urgently needed. Despite considerable advances in traditional disease-modifying anti-rheumatic drugs, anti-inflammatory drugs, anti-cytokines therapy, and Janus kinase inhibitors therapy[4,5], long-term use of these drugs may cause adverse effects, such as gastrointestinal ulcers, myelosuppression, severe infections, and increased risk of cancer. The likelihood of these adverse events increases with the duration and dose of therapy in RA patients, contributing to high treatment cost and limited responsiveness in patients[6,7].

For the management of RA, mesenchymal stem cells (MSCs) present a promising therapeutic option[8–10]. Due to their distinctive immunosuppressive properties, paracrine capacity, and broad availability, MSCs are increasingly utilized in the clinical management of autoimmune conditions[11,12]. Notably, the intravenous administration of therapeutic cells initially results in their entrapment in lung capillaries, which not only reduces homing efficiency, but may also induce severe complications, such as pulmonary embolism[13].Additionally, the unnecessary differentiation of MSCs and the potential malignant transformation have been identified as the most critical safety concerns in MSCs transplantation therapy[14–16]. The inability to control cell fate within body, including the secretion of unwanted factors or the differentiation into undesired cell types post-transplantation, significantly restricts the predictability and reproducibility of treatment outcomes[17].

As introduced previously, stable CCR2 expression in MSCs has been demonstrated to significantly enhance their migratory capacity toward the cognate ligand CCL2[18]. Transfection of CCR2 may consequently potentiate the homing ability of MSCs for therapeutic applications in rat RA models. Furthermore, multiple studies indicate that the immunomodulatory function of MSCs is neither inherent nor static, but rather dynamically regulated by the inflammatory microenvironment[19]. Key inflammatory cytokines, such as IFN-γ can enhance MSCs immunosuppressive capabilities through upregulated chemokine expression and inducible nitric oxide synthase (iNOS) induction. Therefore, targeted upregulation of cytokine expression

[1]State Key Laboratory of Primate Biomedical Research, Institute of Primate Translational Medicine, Kunming University of Science and Technology, Kunming, Yunnan, China. [2]Southwest United Graduate School, Kunming, Yunnan, China. [3]Center for Clinical Medicine Research, The First People's Hospital of Yunnan Province, Kunming, China. [4]These authors contributed equally: Yue Sui, Zixi Pu, Naixue Yang. ✉e-mail: yanyp@lpbr.cn; siw@lpbr.cn

via genomic modification techniques could facilitate site-directed trafficking of systemically administered engineered MSCs to inflamed tissues, thereby enhancing the therapeutic efficacy of conventional MSCs therapies. But compared to conventional MSCs, genetically engineered MSCs raise additional clinical safety concerns, including potential unforeseen side effects and long-term impacts, while their genomic modifications also pose significant challenges for regulatory approval[20]. Using these inflammatory cytokines alone for RA treatment has been shown to be safe but primarily demonstrates a short-term effect in suppressing the immune response and there is insufficient evidence to demonstrate that these inflammatory factors can promote cartilage repair and regeneration[6,21,22]. However, these treatments are costly, exhibit poor stability, have a short shelf life, and may inadvertently promote undesirable differentiation or proliferation of joint tissues. Injection inflammatory cytokines alone limitations hinder their widespread clinical application.

A recent study has revealed that biotechnological methods, such as density gradient centrifugation, can produce enucleated cells that function as carriers of relevant factors[18]. Unlike previous transport vectors, such as extracellular vesicles and nanoparticles[23,24], enucleated cells retain essential cellular organelles and their functions, including endothelial adhesion and homing ability. Consequently, these enucleated cells maintain their paracrine ability and exhibit improved responsiveness to inflammation and the immune microenvironment. Furthermore, genetic modification can further enhance the efficacy of enucleated cells as carriers for precise targeted therapy in damaged tissues, facilitating better delivery to affected tissues and ultimately ameliorating pathological features of diseases[8,25]. The absence of nuclei in the enucleated cells also diminish their inherent tendency to undergo malignant differentiation and uncontrolled proliferation.

RA is characterized by chronic synovial inflammation, with fibroblasts and macrophages predominating over extended periods. Recent single-cell sequencing (scRNA-seq) analyses have illuminated that RA primarily involves the proliferation and activation of lining/sublining fibroblast-like synoviocytes (FLS), the influxes of synovial tissue myeloid cells (STM) into inflammatory synovial tissue, the production of pro-inflammatory cytokines and chemokines, and the invasion of adjacent joint cartilage and bone[26–29]. Throughout the progression of RA, subpopulations of synovial fibroblasts and myeloid cells undergo substantial alterations mediated by various inflammatory factors and pathways[30,31]. However, direct evidence regarding the phenotypic changes and functional heterogeneity of synovial cells following MSCs treatment remains limited. Moreover, the physiological relationships and interactions among these cell types during MSCs or genetically engineered MSCs transplantation are still poorly understood. Unraveling these underlying mechanisms could provide critical insights into the regulation of inflammation and pave the way for more effective tissue repair therapies.

Therefore, in this study, we engineered En-MSCs$^{C/I}$ to co-express CCR2 and IFN-γ, aiming to enhance both homing capacity and local immunomodulatory effects while minimizing risks associated with nuclear content. We evaluated their therapeutic efficacy in a rat model of RA and explored potential downstream mediators of their action. Among the candidate effector molecules, SEMA3E known for its roles in immune regulation and vascular remodeling[25,32,33], was identified as a promising factor enriched in En-MSC$^{C/I}$ treated synovial tissues. Although the precise mechanisms of SEMA3E action remain to be fully characterized, we conducted preliminary in vivo experiments using recombinant SEMA3E protein to assess the possible involvement of SEMA3E in mediating their beneficial effects.

Results

En-MSCs$^{C/I}$ retained essential organelles and cellular functions

The identity of isolated hUC-MSCs was confirmed through immunophenotype profile assessment and the differentiation assays into adipocytes, osteoblasts, and chondrocytes (Fig. S1A). The stable and elevated expression of CCR2 and IFN-γ in MSCs was achieved by lentiviral transfection (Fig. S1B). Then cell nuclei were physically removed by using cytorelaxin B in conjunction with Ficoll density gradient ultracentrifugation (Fig. 1A). The En-MSCs$^{C/I}$ was suspended in the penultimate layer after centrifugation and retained the ability to attach to tissue culture plates, showing substantially smaller size compared to untreated MSCs (Fig. 1B and Fig. S1C). The cytoskeletal structure of En-MSCs$^{C/I}$ was well organized after adhering to the culture dish for 48 h (Fig. 1C). Transmission electron microscopy confirmed that the nuclei of En-MSCs$^{C/I}$ was absent, while other essential cellular organelles remained intact (Fig. 1D). Flow cytometry analysis to quantify enucleation efficiency showed that the proportion of DAPI-negative cells in En-MSCs$^{C/I}$ reached approximately 96.8%, indicating high enucleation efficiency (Fig. 1E and Fig. S1D). Cell viability of En-MSCs$^{C/I}$ was assessed over a 24, 48, and 72 h period using the Trypan Blue exclusion method in combination with an automated cell counter. A substantial proportion of cells remained viable after enucleation, indicating that En-MSCs$^{C/I}$ retained sufficient membrane integrity and short-term survival capacity to support subsequent regulatory functions. (Fig. 1F). To further confirm successful enucleation, we performed western blot analysis for nuclear envelope proteins (LMNA/C, SUN2) and representative protein (Tubulin, Vimentin, FAK, β-actin). As expected, LMNA/C and SUN2 were few in En-MSCs$^{C/I}$, whereas cytoskeletal proteins remained stably expressed, confirming the presence of corresponding proteins in En-MSCs$^{C/I}$ (Fig. 1G, H and Fig. S1E). To evaluate the stability of the engineered features post-enucleation, we examined the expression of CCR2 and IFN-γ in in pre-enucleated MSCs, MSCs overexpressing CCR2 and IFN-γ (MSCs$^{C/I}$) and En-MSCs$^{C/I}$ at 24 and 48 h post-nucleation by flow cytometry. The results showed that both markers remained highly expressed post-enucleation, with profiles comparable to those observed in pre-enucleated MSCs (Fig. 1I and Fig. S1F). We also assessed whether En-MSCs$^{C/I}$ retained MSCs phenotypic markers after enucleation. Flow cytometry at 24 and 48 h post-enucleation showed that the expression levels of CD44, CD73, and CD90 remained consistently above 90% in both En-MSCs$^{C/I}$ and MSCs, with no significant differences observed between groups at either time points. In addition, the expression of the negative cocktail (CD45, CD34, CD11b, CD19, and HLA-DR) was detected at levels below 5% in both MSCs and En-MSCs$^{C/I}$. These results indicate that En-MSCs$^{C/I}$ retain a stable surface phenotype over time, supporting their equivalence to MSCs (Fig. 1J and Fig. S1G). We performed an in vitro scratch assay to assess the migratory capacity of En-MSCs$^{C/I}$. Results confirmed that even 48 hours post-enucleation, the cells retained migration ability (Fig. S1H and S1I). To further verify the functionality of transfect CCR2, we performed a CCL2-induced transwell chemotaxis assay. The results demonstrated that CCR2 transduction significantly enhanced the migratory capacity of both MSCs$^{C/I}$ and En-MSCs$^{C/I}$ at 6 and 12 h (Fig. S1J and S1K), confirm that CCR2 expression is functionally active and mediates their chemotactic response toward CCL2. These findings indicate that En-MSCs$^{C/I}$ retain stable surface phenotype over time, supporting their equivalence to MSCs. Collectively, these results indicate that enucleated cells retain essential cellular structure and activity.

Both MSCs and En-MSCs$^{C/I}$ ameliorated synovial inflammation in RA rat model

We evaluated the therapeutic efficacy of MSCs and En-MSCs$^{C/I}$ in Type II-Collagen induced arthritis (CIA) rats. The immunological and histological features of the RA rat model closely resemble those observed in clinical RA patients[34,35]. Consequently, four weeks after Type II- Collagen administration, we administered En-MSCs$^{C/I}$ (enucleated hUC-MSCs without lentiviral transfection and overexpressing CCR2 and IFN-γ), En-MSCs$^{C/I}$ (enucleated hUC-MSCs overexpressing CCR2 and IFN-γ), as well as hUC-MSCs to the CIA rats. The transplantation of En-MSCs$^{C/I}$ and MSCs resulted in significant symptom improvements compared to the RA model group (CIA rats administrated with saline), including reduced joint swelling, and decreased rheumatoid score (Fig. 2A, B). The micro-CT scan images revealed evident joint surface destruction in both the RA model group, indicating severe damage to both the joint surface and trabecular bone.

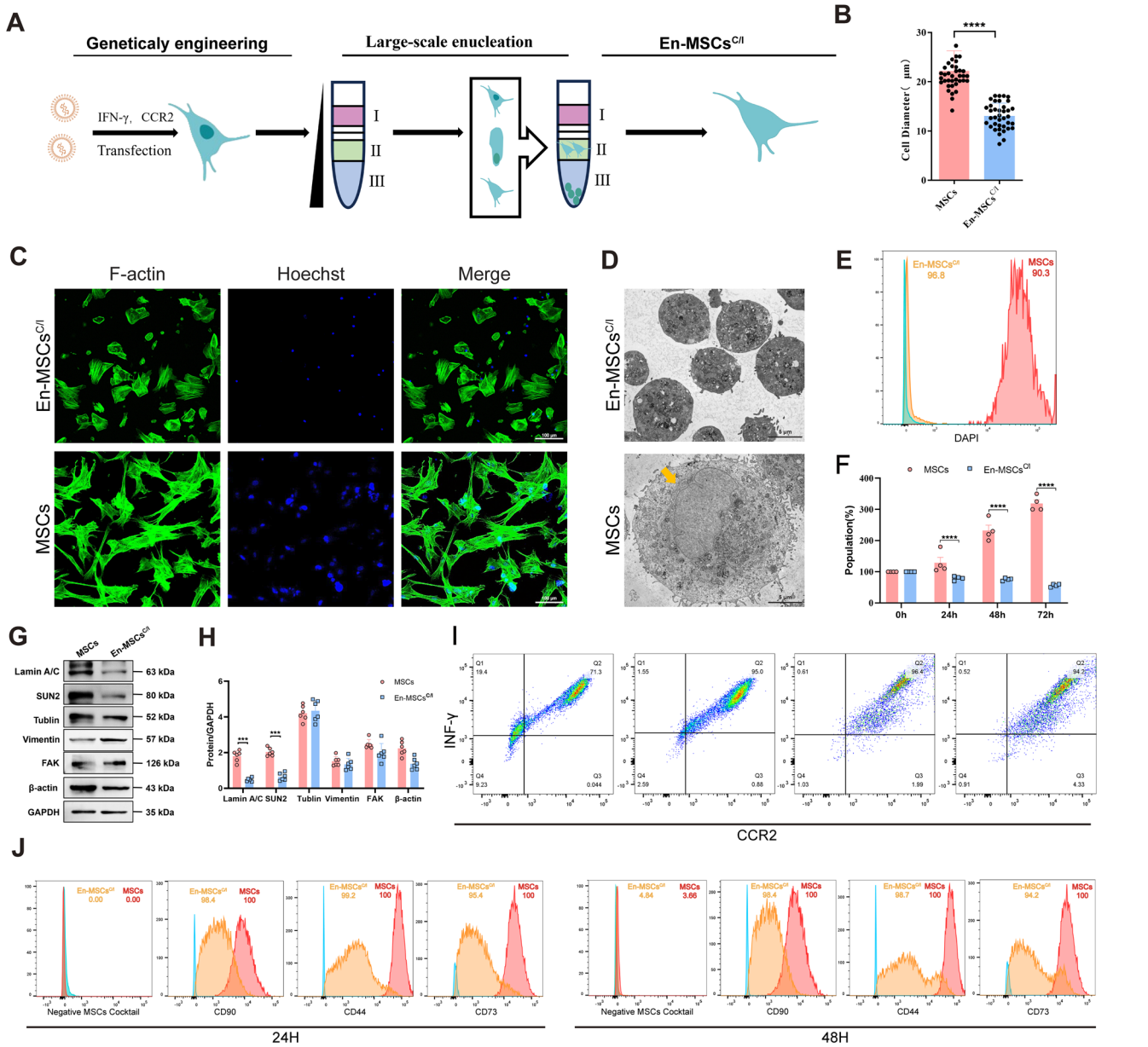

Fig. 1 | En-MSCs$^{C/I}$ retained essential organelles and cellular functions. **A** Schematic of workflow for genetic engineering and enucleation of hUC-MSCs. **B** Average diameter of MSCs or En-MSCs$^{C/I}$. Mean ± s.e.m. (****$p < 0.0001$). **C** Fluorescent confocal images of MSCs and En-MSCs$^{C/I}$ stained with F-actin for cytoskeleton, and Hochest for nucleus. Scale bar = 20 μm. Representative confocal image selected from three independent experiments. **D** Representative Electron microscopy images biologically independent samples of MSCs and En-MSCs$^{C/I}$. Yellow arrow pointed to typical cell nucleus in MSC, Scale bar, 5 μm. **E** Flow cytometry analysis of DAPI staining post-enucleation. Compared to MSCs, En-MSCs$^{C/I}$ exhibited a DAPI-negative population of approximately 96.8%. **F** Quantification of En-MSCs$^{C/I}$ viability at 0, 24, 48, and 72 h post-enucleation using the Trypan Blue exclusion method. Data represent the percentage of viable (unstained) cells measured by automated cell counter. Mean ± s.e.m. ($n = 3$, ***$p < 0.0001$). **G** Western Blot of LMNA/C, SUN2, Tublin, Vimentin, FAK, β-actin, and GAPDH in MSCs and En-MSCs$^{C/I}$ after 24 hours of adherence. The molecular weight marker (kDa) are shown. GAPDH served as the loading control. Lane order and sample identities are indicated on the blots. **H** Quantiffcation of the Western blot analysis. Data are represented as the Mean ± s.e.m. ($n = 6$, ***$p < 0.001$). **I** Flow cytometry analysis of CCR2 and IFN-γ expression in MSCs, MSCs$^{C/I}$, En-MSCs$^{C/I}$ at 24 and 48 h post-enucleation (from left to right). **J** Flow cytometry showing expression of negative cocktail, CD44, CD73, and CD90 at 24 and 48 h post-enucleation. All error bars denote Mean ± s.e.m.; dots indicate individual samples.

Conversely, the CIA rats treated with En-MSCs$^{C/I}$ and MSCs exhibited a significantly improvement in joint destruction assessed by radiological assessments, with near-complete restoration of joint morphology (Fig. 2C). Moreover, comparison to the RA model group, the En-MSCs$^{C/I}$ and MSCs group exhibited reduced levels of RF, CRP, IL-1β and TNF-α in the serum of the rats (Fig. S2A). Histological assessment and inflammation scoring revealed that En-MSCs$^{C/I}$ significant reduction knee synovial immune cell infiltration and inflammation (Fig. 2D, E). Immunohistochemistry confirmed decreased TNF-α and iNOS expression in the En-MSCs$^{C/I}$ group compared to the RA model group. Indicating enhanced anti-inflammatory effects (Fig. 2D, F). The pathological results of En-MSCs$^{C/I}$ was consistent with those of MSCs, whereas En-MSCs exhibited mild improvements in immune cell infiltration and joint destruction.

We next aimed to determine whether i.v. administered En-MSCs$^{C/I}$ can more effectively home to sites of inflammation in vivo. CIA rats were intravenously injected with GFP-labeled En-MSCs, En-MSCs$^{C/I}$ or MSCs. Bioluminescence analysis demonstrated enhanced signals at the hind limb joints in the CIA rats administrated with En-MSCs$^{C/I}$ at 24, 48, and 72 h post

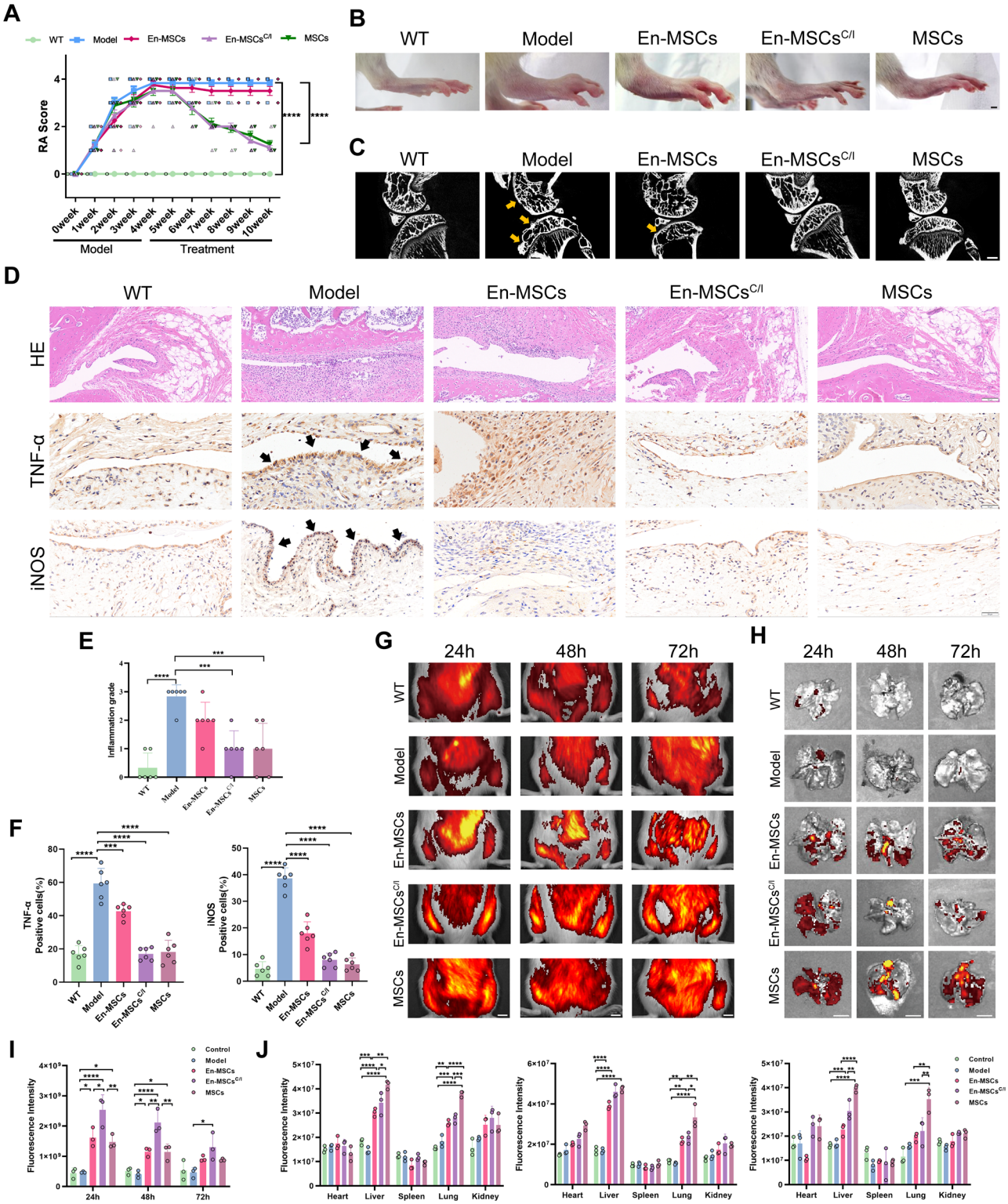

Fig. 2 | Both MSCs and En-MSCs$^{C/I}$ ameliorate synovial inflammation in CIA Rats. A Arthrosis severity was continuously monitored, and the arthritis scores were calculated until sacrifice. Mean ± s.e.m. ($n = 6$ per group, $^{**}p < 0.01$, $^{***}p < 0.001$, $^{****}p < 0.0001$). **B** Representative photographs of hind paws taken 6 weeks post-injection. Scale bar = 2 mm. **C** Micro-CT images of knee joint sagittal sections from different treatment groups. Yellow arrows indicated bone erosion on the tibial plateau. Scale bar = 1 mm. **D** Representative histological images of inflammatory infiltration in knee joint synovium by H&E and Immunohisto-chemical staining for TNF-α and iNOS, and arrows indicated high expressing levels. Scale bar = 50 μm. **E** Inflammation grade based on analysis of synovial hyperplasia, inflammatory cell infiltration. ($n = 6$ per group, $^{***}p < 0.001$, $^{****}p < 0.0001$). **F** iNOS+ and TNF+ chondrocytes were quantified. ($n = 6$ per group, $^{***}p < 0.001$, $^{****}p < 0.0001$). **G** Representative Fluorescence imaging of knee joints of rats administrated with different group at indicated time points. Scale bar = 1 cm. **H** Representative Fluorescence imaging from three animals per group of lungs of rats administrated with different group at indicated time points. Scale bar = 1 cm. **I** Quantitative analysis of the fluorescence intensity and its temporal changes in the joint of rats with different group. ($n = 3$ per group, $^{*}p < 0.05$, $^{**}p < 0.01$, $^{****}p < 0.0001$). **J** Quantitative analysis of the fluorescence intensity and its temporal changes in the major organs of rats with different group. ($n = 3$ per group, $^{*}p < 0.05$, $^{**}p < 0.01$, $^{***}p < 0.001$, $^{****}p < 0.0001$). All error bars denote Mean ± s.e.m; dots indicate individual samples/rats.

injection, indicating that En-MSCs$^{C/I}$ to efficiently home to the target tissues in vivo compared to the En-MSCs and MSCs group (Fig. 2G, I). Consequently, the intensity of excised lungs, livers, spleens, hearts and kidneys from the CIA rats injected with En-MSCs, En-MSCs$^{C/I}$ or MSCs were assessed to evaluate the extent of cell integration into these tissues at these time points. The bioluminescence assay showed accumulation of En-MSCs, En-MSCs$^{C/I}$ and MSCs in various organs. Notably, the En-MSCs and En-MSCs$^{C/I}$ group displayed reduced signals in the lungs compared to the MSCs group, demonstrating that MSCs preferentially accumulated in pulmonary veins rather than effectively migrating to the injured joints (Fig. 2H, J and Fig. S2B).

Finally, we observed no adverse effects or mortality in the CIA rats administrated with MSCs and En-MSCs$^{C/I}$ over a 3-month period. Additionally, no pathological changes were detected in major organ tissues, as assessed by H&E staining (Fig. S3). These findings indicate that systemic administration of En-MSCs$^{C/I}$ effectively alleviated joint swelling and synovial hyperplasia in CIA rats via reducing inflammation, and demonstrate favorable safety profiles, akin to the therapeutic effects of MSCs.

MSCs and En-MSCs$^{C/I}$ modulate the immune and inflammatory processes of FLS and STM to ameliorate synovitis

To determine the phenotypic spectrum of cell subtypes in rat synovial tissues, we employed scRNA-seq to analyze samples from the WT group, RA model group and RA model treated with MSCs or En-MSCs$^{C/I}$. Total of 103,406 cells extracted from complete synovial tissues were subjected to downstream analysis, and six distinct cell subtypes were confidently identified based on the differentially expressed genes within each cell cluster (Fig. S4A). Representative genes for each cluster mapped onto the UMAP plots, demonstrated the distinctly different nature of each major cell type. The six cell subtypes were endothelial cells (EC), fibroblast-like synoviocytes (FLS), STM, vascular smooth muscle and cells (VSMC), lymphocytes (Lym). The majority of acquired FLS were synovial sublining fibroblasts (SSF) and synovial lining fibroblasts (SLF). A list of genes was collected upon literature research (Supplementary Data 1). The SSF were characterized by the expression of stromal cell-derived factor 1 (*Cxcl12*), which are involved in synthesis, while the SLF expressed genes essential for the production of synovial fluid components, such as lubricin (*Prg4*). Other canonical gene markers applied were *Emcn* and *Cdh5* for EC, *Acta2* and *Tagln* for VSMC, *C1qa* and *Lyz2* for STM, *CD3d* and *CD3e* for Lym (Fig. S4B).

Previous study has indicated that sublining and lining FLS and STM are predominantly present in healthy synovium (Fig. S4C). In RA patients, however, there is a drastic increase in the numbers of both sublining and lining FLS and STM[36]. Then, we further investigated whether FLS or STM populations contributed to the amelioration of synovitis during MSCs or En-MSCs$^{C/I}$ treatment. Through cluster correlation assessment, we defined four distinct states in sublining and lining FLS, with one cluster (interim sublining) representing an intermediate state among the states (Fig. 3A). In each synovial sublining and lining FLS cluster, there was distinct state known as "activated" that is linked to inflammatory responses and cytokine signaling, while the contrasting state lacking these characteristics is termed "resting"[26]. The activated lining FLS, marked by increased expression of *CD74* and *RT1-Da*, was characterized by antigen processing and presentation and inflammatory response, reflecting their unique functions in RA synovial tissue. Similarly, the activated sublining FLS exhibited high expression of *Cxcl12* and *Mmp14* genes, with functions associated with transcriptional regulation (Fig. S4D and Fig. 3B).

We further identified four subtypes of STM in synovial tissues, including Trem2+ macrophage (*Trem2, Apoe, Vsig4*), Clec10a+ macrophage (*Clec10a, Gpr183, Ccl4*), Cebpb+ macrophage (*Cebpb, Clec7a, Ccr5*), and Hbegf+ monocyte (*Hbegf, Egr1, Ly6c*) (Fig. 3C and Fig. S4D). The Hbegf+ monocyte cluster, enriched in extracellular matrix, blood vessel development, and growth factor-related signaling pathway, might be associated with the abnormal proliferation of blood vessels and EC during RA progression (Fig. 3D). GO analysis indicated that Trem2+ macrophage cluster displayed distinct metabolic and endocytosis regulatory features, including the upregulation of lipid-binding proteins that modulate metabolism (Apoe) and suppression of T effector cells (Vsig4), potentially contributing to local regulation of adaptive immune response. The cluster with high expression of Clec10a+ was associated with inflammation and immune signal transduction (Gpr183 and Ccl4) (Fig. 3D and Fig. S4D).

RA induced significant changes in both proportion and abundance of these subsets, the resting lining and sublining FLS were predominant in healthy synovial tissue, the abundance of activated lining FLS increased significantly in model group and resume to normal levels in the MSCs group and En-MSCs$^{C/I}$ group (Fig. 3E and Fig. S4E). The most robust increases were observed in the Hbegf+ cluster within the model group, which exhibited distinct monocyte characteristics. Treatment with either MSCs or En-MSCs$^{C/I}$ resulted in a significant reduction in the number of Hbegf+ monocytes, bringing their levels down to those observed in the control group (Fig. 3E and Fig. S4F). Additionally, inflammation scores were assessed for all groups, showing a significant increase for the activated lining FLS and Hbegf+ monocytes in the model group. However, these scores decrease following treatment (Fig. 3F). Heatmaps illustrating the scaled enrichment of most immune and inflammation-related factors, as well as transcription factors in activated lining FLS and Hbegf+ monocytes, remained consistent patterns across both the MSCs group and the En-MSCs$^{C/I}$ group (Fig. S4G). Subsequently, immunofluorescence assay confirmed the high expression levels of Cd74 and Hbegf in the model group (Fig. S5A and S5B), indicating that the amelioration of RA synovial inflammation by the treatment of MSCs and En-MSCs$^{C/I}$.

After identifying distinct FLS and STM and their abundance in synovial tissues, we assessed whether their transcriptomic profiles underpinned distinct functional roles following the treatment with MSCs and En-MSCs$^{C/I}$ in CIA rats. Activated lining and activated sublining clusters in both the MSCs group and En-MSCs$^{C/I}$ group exhibited similar features, particularly in the roles in reducing immune and inflammatory responses (Fig. 3G). The subsets of STM were also subjected to GO analysis to characterize their function patterns under the treatment of MSCs or En-MSCs$^{C/I}$. Both Hbegf+ monocytes and Cebpb+ macrophages in the En-MSCs$^{C/I}$ and MSCs groups exhibited similar reductions in the modulation of angiogenesis, signal transduction and immune and inflammatory responses (Fig. 3H). In the En-MSCs$^{C/I}$ group, STM exhibited a higher proportion of Trem2+ cluster. GO analysis revealed that the En-MSCs$^{C/I}$ group showed greater enrichment in lipid and protein metabolism and endocytosis functions. Additionally, Trem2+ macrophages were more uniformly distributed within the lining layer, indicating their superior barrier protection function (Fig. S6A and S6B). This indicates that En-MSCs$^{C/I}$ may leverage the barrier capacity and metabolic regulation of the Trem2+ cluster to modulate synovial inflammation and immune infiltration in the CIA rats. Overall, these results demonstrate that both MSCs and En-MSCs$^{C/I}$ possessd similar capabilities in reducing vascular proliferation within the synovium, ameliorating synovial inflammation, and modulating the immune microenvironment by regulating activated lining and sublining FLS, as well as Hbegf+ and Cebpb+ STM. In vitro transwell co-culture experiments with LPS stimulated synoviocytes showed that inflammation-related gene mRNA levels were downregulated. Specifically, the expression of *IL-1β, TNF-α, Ccl2, Cxcl12* and *Mmp1* was significantly lower in both the En-MSCs$^{C/I}$ group and the MSCs group compared to the LPS group (Fig. S6C).

To explore the impact of MSCs and En-MSCs$^{C/I}$ on RA synovitis pathology via activated lining FLS and Hbegf+ monocytes, we focused on their intercellular interactions. Hbegf+ monocytes are known to participate in the communication system between inflammatory monocytes and fibroblasts[29]. The crosstalk involving activated lining FLS and Hbegf+ monocytes might drive inflammatory cell aggregation, pro-inflammatory factor secretion, and excessive immune response in the RA model group. By utilizing CellChat, we identified crucial ligand-receptor pairs involved in signaling between activated lining FLS and HBEGF+ monocytes (Fig. 3I). The primary interacting pairs included *Cxcl13, Csf, Cxcl12, Spp1, Hbegf* and

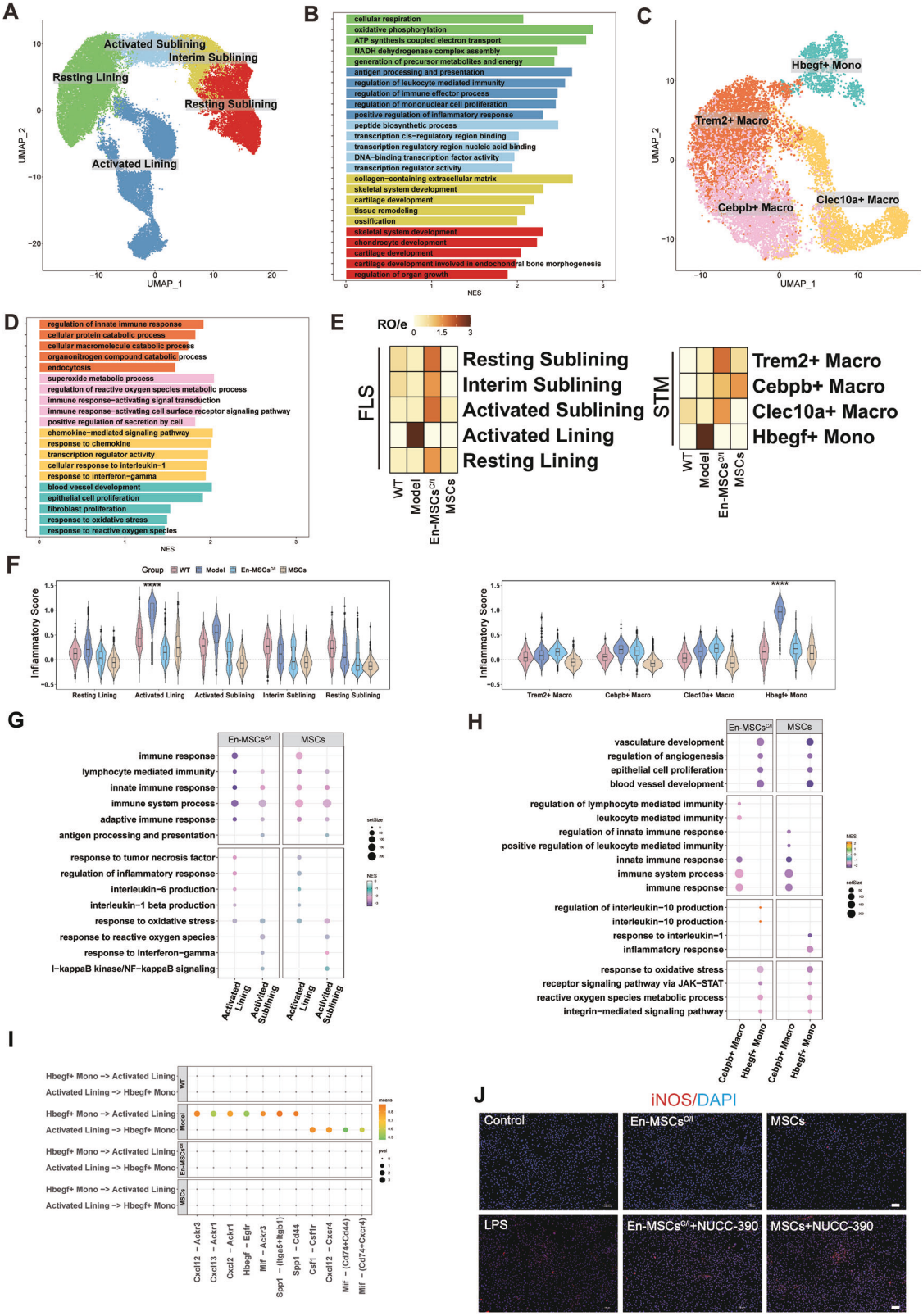

Fig. 3 | MSCs and En-MSCs$^{C/I}$ modulate the immune and inflammatory processes of FLS and STM to ameliorate synovitis. A UMAP visualization of heterogeneity of FLS. **B** GSEA showing the cellular functions of different FLS clusters. **C** UMAP visualization of heterogeneity of STM. **D** GSEA showing the cellular functions of different STM clusters. **E** Heatmap showing the odds ratios (ORs) of FLS and STM clusters in each group. OR > 1.5 indicated a preferential distribution of the cluster within the corresponding tissue. **F** Inflammatory scores of clusters in different groups. *p*-value were calculated by the Mann-Whitney U test, $****p < 0.0001$. **G** GSEA showing the cellular functions of immune and inflammatory of activated ling and activated sublining FLS regulated by MSCs and En-MSCs$^{C/I}$ administration. **H** GSEA showing the cellular functions of immune and inflammatory of Hbegf+ and Cebpb+ STM regulated by MSCs and En-MSCs$^{C/I}$ administration. **I** Significant ligand-receptor pairs that contributed to cellular crosstalk between activated Lining FLS and Hbegf+ monocytes. The dot color and size represented the calculated communication probability and *p*-value. *p*-value were computed from one-sided permutation test. **J** Representative confocal microscopy of iNOS (red) and DAPI (blue) from synovial tissue of different groups. Scale bars, 100 μm.

Mif, which promoted neutrophil aggregation and stimulate downstream inflammatory factor secretion, leading to RA pathogenesis (Fig. S6D). Notably, these typical interacting pairs were absent in the control and treatment groups, indicating that MSCs and En-MSCs$^{C/I}$ might mitigate inflammatory cell cluster crosstalk by inhibiting these factors, thereby reducing inflammation and ameliorating joint synovitis.

Cxcl12 is an inflammatory chemokine, while Cxcr4 serves as its specific receptor. Subsequently, we investigated the impact of Cxcl12-Cxcr4 axis on the treatment of synovial inflammation with MSCs and En-MSCs$^{C/I}$. Primary synoviocytes were stimulated with LPS for 24 hours. Subsequently, during treatment with En-MSCs$^{C/I}$ or MSCs, the CXCR4 agonist NUCC-390 was added. Expression of iNOS was then assessed via immunofluorescence staining. The observed increase in iNOS expression upon NUCC-390 treatment confirmed the targeted role of CXCR4 in mitigating synovial inflammation (Fig. 3J and Fig. S6E and S6F). These findings suggest that MSCs and En-MSCs$^{C/I}$ might suppress the Cxcl12-Cxcr4 axis to disrupt crosstalk between FLS and STM, and thereby mitigating synovial inflammation.

En-MSCs$^{C/I}$ exhibited unique regulatory signatures for tissue regeneration

Both MSCs and En-MSCs$^{C/I}$ exhibit similar regulatory functions in immune and inflammatory environments. The treatment with En-MSCs$^{C/I}$ led to a notable decrease in the number of activated lining FLS, accompanied by a significant increase in the resting lining and resting sublining populations, and displayed unique transcriptome features (Fig. 3E). The resting lining FLS were characterized by high expression of genes associated with ECM production (*HAS1*) and complement system regulation (*CD55*), with functional enrichment primarily related to ATP generation and metabolism. Conversely, the resting sublining FLS exhibited characteristics of progenitor cell, including elevated levels of *CD34* and *THY1* expression, which contribute to ECM stability and the development of joint cartilage or bone (Fig. 4A). Through pseudotime plot analysis for trajectory assessment, we identified a trajectory node at the resting sublining FLS, which served as the starting point of pseudo-time trajectory (Fig. 4B). This further supports the hypothesis that the resting sublining FLS may possess characteristics of stem cells or early progenitor cells. Immunofluorescence confirmed the high expression levels of CD34 in the En-MSCs$^{C/I}$ group (Fig. 4C and Fig. S7A). Therefore, elevation in the resting lining of synovial tissue may be essential for the repair of joint damage in RA.

Differential gene analysis revealed significant enrichment of Gas6, Sox5, TGF-β and BMP family members in the resting lining FLS from the En-MSCs$^{C/I}$ group, and these genes facilitated the regeneration and repair processes of articular cartilage and osseous tissue (Fig. 4D). Furthermore, the resting lining FLS from the En-MSCs$^{C/I}$ group demonstrated typical involvement in the growth hormone synthesis, secretion and action, enrichment of FoxO signaling, Wnt signaling and ECM-related pathways, suggesting their potential role in tissue remodeling and homeostasis. Meanwhile, the resting lining FLS from the MSCs group demonstrated typical involvement in NFκB, TLR, TGF-β and mTOR signaling pathway through KEGG analysis (Fig. 4E and Fig. S7B). Then, we further evaluated the typical functions related to joint development and regeneration in the resting lining FLS. The GSNE map indicated that the Wnt signaling pathway, stem cell differentiation, and processes related to cell and tissue development and remodeling were expressed at significantly higher levels in the En-MSCs$^{C/I}$ group compared to the MSCs group (Fig. 4F, G). Following the pathway and functional enrichment analyses, we selected cartilage regeneration related genes for targeted validation by qRT-PCR in synovial tissue, including *SOX5, SOX9, GAS6, TGFB2, FGF, COMP*, and *IGF1*. The results show that En-MSCs$^{C/I}$ treatment significantly increased the expression of these genes in synovium relative to RA and also differed from the MSC group, aligning with the regulatory signatures predicted (Fig. 4H). These results suggested that En-MSCs$^{C/I}$ might offer enhanced therapeutic effects for joint deficiencies arising from RA through the resting FLS.

En-MSCs$^{C/I}$ exhibited enhanced therapeutic potential on cartilage regeneration in vitro and in vivo

Subsequently, we induced cellular damage in rat primary articular chondrocytes using H_2O_2 in vitro, and the immunofluorescence results revealed that damaged chondrocytes exhibited reduced expression of Ki67 and diminished proliferative capacity (Fig. 5A, B). In comparison to the cell administrated with H_2O_2, the chondrocytes treated with either En-MSCs$^{C/I}$ or MSCs showed increased expression of Ki67, with a higher level observed in the chondrocytes treated with En-MSCs$^{C/I}$ than those with MSCs. Furthermore, when the complete culture medium of synovial cells was co-cultured with H_2O_2 damaged chondrocytes along with either En-MSCs$^{C/I}$ or MSCs in vitro, a further increase in Ki67 expression was observed compared to those treated solely with MSCs or En-MSCs$^{C/I}$. Notably, the proliferation of chondrocytes was most pronounced in the damaged chondrocytes treated with En-MSCs$^{C/I}$ combining with synovial culture medium (Fig. 5B, C and Fig. S8A), indicated that En-MSCs$^{C/I}$ or MSCs effectively enhance the proliferation of chondrocytes via synovial cells. We further compared the therapeutic effects of En-MSCs$^{C/I}$ and MSCs in the context of cartilage damage. In vitro transwell co-culture experiments with damaged chondrocytes showed upregulated mRNA levels of cartilage-related markers after 48 hours, with higher expression of *ACAN* and *COL2* in the En-MSCs$^{C/I}$ group compared to the MSCs group (Fig. 5D, Fig. S8B and S8C). The CIA rats with extensive synovial tissue proliferation invading the cartilage surface were administrated with MSCs or En-MSCs$^{C/I}$ at 8 weeks post-Type II collagen induction. Pathological analysis of the CIA rats before cell transplantation revealed severe cartilage destruction, both the MSCs and En-MSCs$^{C/I}$ treatment groups exhibited restoration of smooth and intact joint cartilage surface, as evidenced by toluidine blue and fast green staining indicating improved joint cartilage compared to the RA model group (Fig. 5D, G). Immunohistochemical staining demonstrated enhanced COL2 and ACAN expresssion in the En-MSCs$^{C/I}$ treatment group comparable to the MSCs group, suggesting that regenerated cartilage from En-MSCs$^{C/I}$ transplantation resembled normal rat hyaline cartilage rather than mechanically inferior fibrous or hypertrophic cartilage (Fig. 5F, H). Furtherly, immunofluorescence staining showed upregulated levels of COL2 in the En-MSCs$^{C/I}$ group compared to the MSCs group. These results demonstrate that En-MSCs$^{C/I}$ was superior at promoting repair and proliferation of damaged chondrocytes.

Administration of SEMA3E ameliorated synovial inflammation and cartilage damage in CIA rats

En-MSCs$^{C/I}$ and MSCs ameliorate synovial inflammation by upregulating the Trem2, Clec10a, and Cebpb macrophage clusters. We further investigated the interactions among these clusters and their implications for downstream cartilage repair (Fig. 6A). In the En-MSCs$^{C/I}$ group, we observed constitutive ligand-receptor interactions associated with these clusters, some of which were consistent with the control group but absent in the model group. The primary interaction pairs included members of the Fgf, col, itgb2, Sema, and Bmp families. Principal function enrichment analysis revealed that these factors were closely linked to stem cell differentiation, as well as cartilage and bone development and regeneration (Fig. 6B, C). Notably, these typical interaction pairs were not observed in the MSCs group, indicating that intercellular communication in the En-MSCs$^{C/I}$ group may be a pivotal factor in promoting joint repair and regulating tissue regeneration compared to the MSCs group. Among these interactions, factors from Sema families have been demonstrated to play a crucial role in modulating function, inflammation, and immune response during various stages of host defense against immune cells regulation[37]. We also noted a decrease in SEMA3E expression in the sublining FLS within the model group, which was restored to normal levels in the En-MSCs$^{C/I}$ group (Fig. 6B). In addition, the administration of SEMA3E to CIA rats reduced hind paw swelling and prevented synovial membrane proliferation and significant cartilage defects after 4 weeks. (Figs. 6D and 6E). Toluidine blue and Fast Green staining revealed intact joint surfaces with significantly cartilage restoration compared to the CIA rats from model group

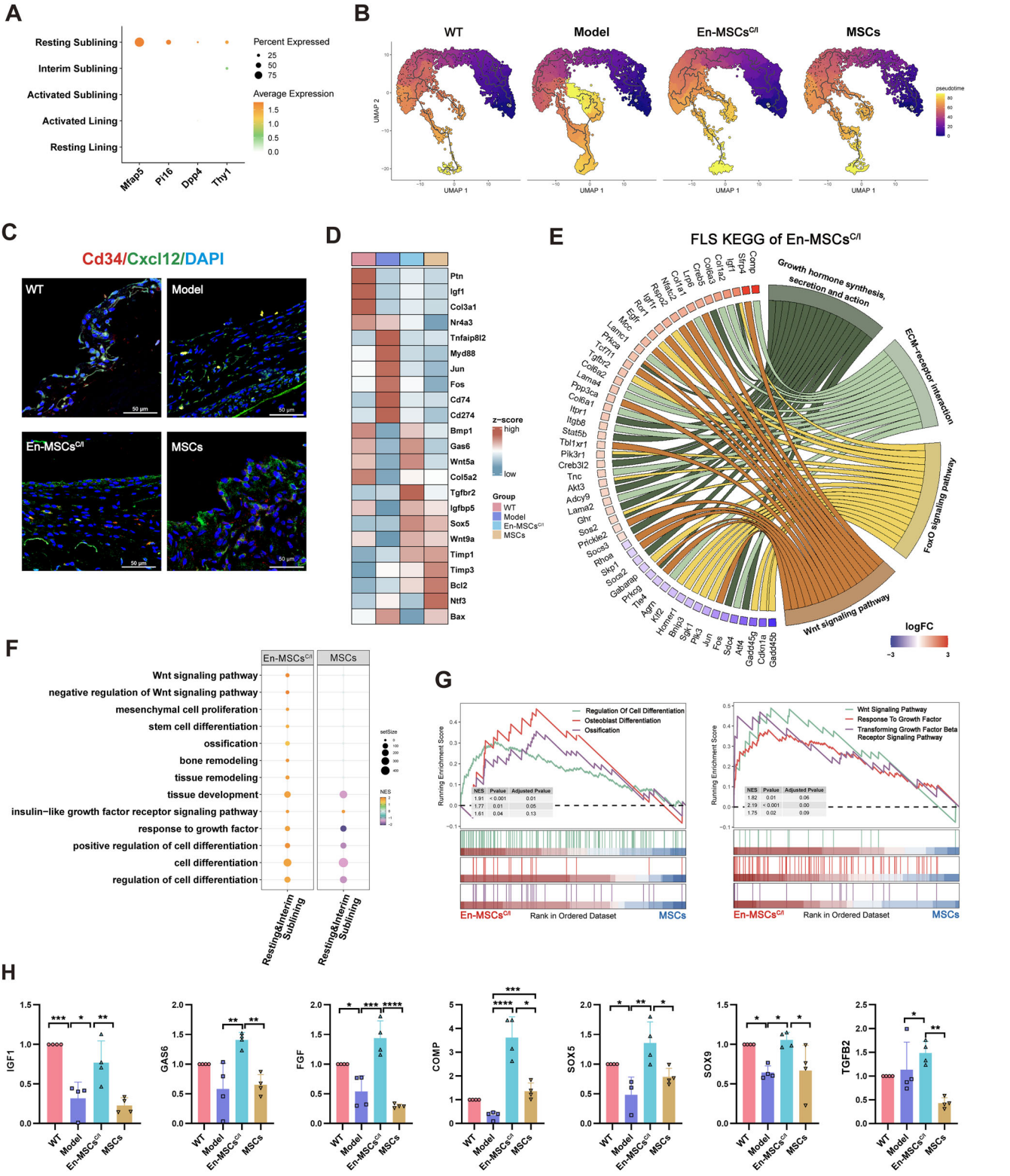

Fig. 4 | En-MSCs$^{C/I}$ exhibited unique regulatory signatures for tissue regeneration. A Dot plots showing the expression levels of tissue progenitors and 'stem-like' cells genes for each cluster of FLS. **B** Resting sublining served as the starting point of pseudo-time trajectory. **C** Representative confocal microscopy of CD34 (red) and CXCL12(green) in synovial tissues from different group, and arrows indicated CD34 expression in resting sublining FLS from the En-MSCs$^{C/I}$ group. Scale bars, 50 μm. **D** Heatmaps illustrating scaled expression of the top marker genes of FLS within the four groups. **E** Kyoto Encyclopedia of Genes and Genomes (KEGG) pathways showing fibroblasts clusters functional differences between the En-MSCs$^{C/I}$. **F** GSEA showing differences in tissue development and regeneration function of resting&-interim sublining FLS between the MSCs group and the En-MSCs$^{C/I}$ group. **G** GSEA plot of differentiation pathways enrichment in resting&interim sublining treated with En-MSCs$^{C/I}$ versus MSCs. NES, normalized enrichment score. **H** qRT-PCR analysis of cartilage regeneration–associated genes (IGF1, GAS6, FGF, COMP, SOX5, SOX9, TGFB2) in synovial tissue after treatment. Gene expression was normalized to GAPDH. Mean ± s.e.m. (n = 4 per group, $^{*}p < 0.05$, $^{**}p < 0.01$, $^{***}p < 0.001$, $^{****}p < 0.0001$). All error bars denote Mean ± s.e.m.; dots indicate individual samples.

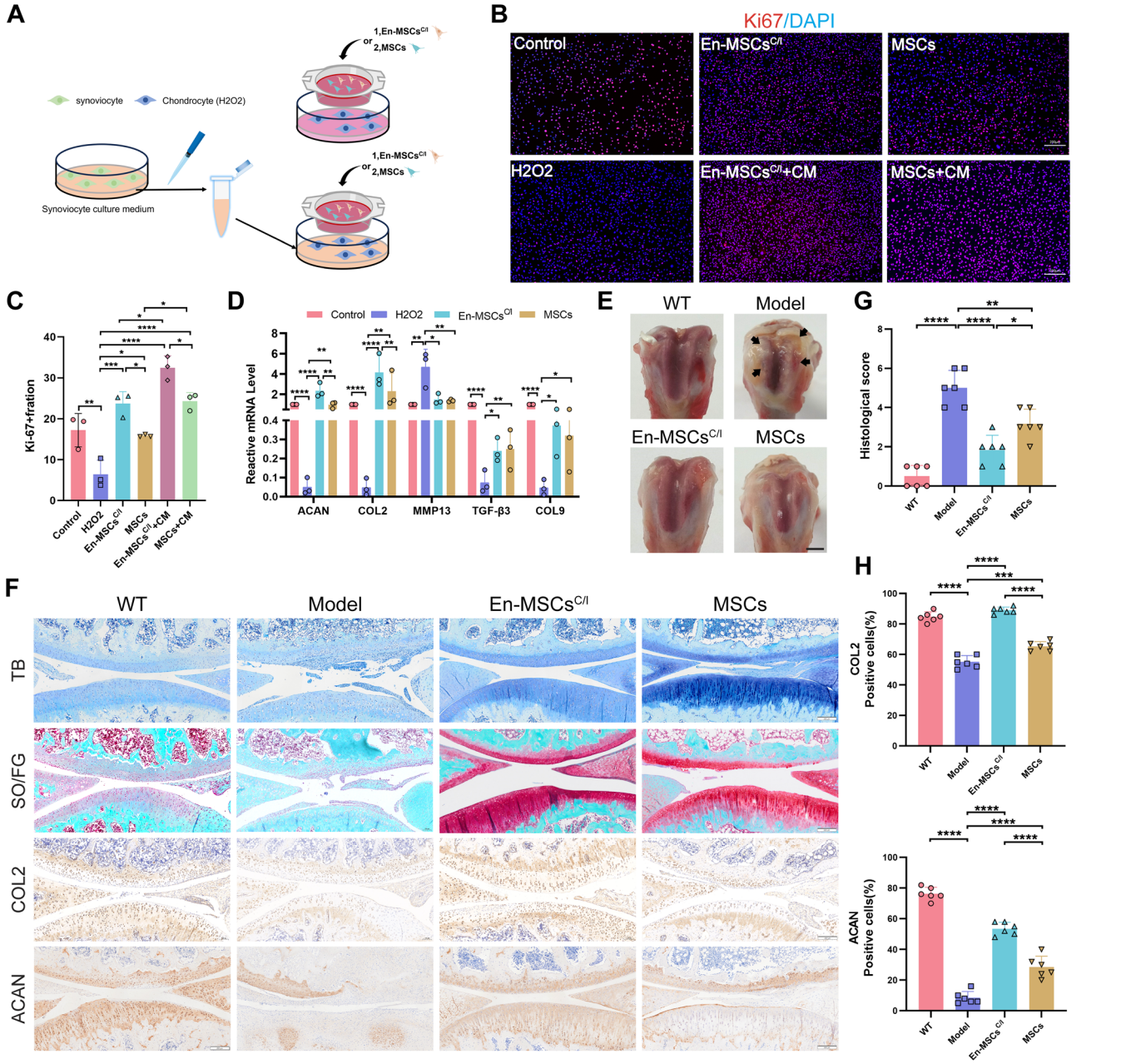

Fig. 5 | En-MSCs$^{C/I}$ exhibited enhanced therapeutic effects on cartilage regeneration. A Schematic diagram of the transwell assay showing the therapeutic effects of En-MSCs$^{C/I}$ and MSCs on damage chondrocytes in vitro. **B** Fluorescence imaging of Ki67 (red) demonstrating the effects of different treatments on damage chondrocytes in vitro. Scale bar = 200 μm. **C** Immunofluorescence statistical analysis of Ki67 levels in chondrocytes from different treatments. **D** qPCR analysis of cartilage development-related genes in different groups. Mean ± s.e.m. ($n = 3$ per group, $^{*}p < 0.05$, $^{**}p < 0.01$, $^{***}p < 0.001$, $^{****}p < 0.0001$). **E** Representative knee morphologies from n = 6 independent CIA rats treated with MSCs or En-MSCs$^{C/I}$ for 6 weeks. Arrows indicating obvious cartilage damage and synovial hyperplasia. Scale bar = 2 mm. **F** Representative pathological images of cartilages treated with En-MSCs$^{C/I}$ or MSCs. Joints were stained with safranin O, toluidine blue, and immunohistochemical staining for ACAN and COL2. Scale bar = 200 μm. **G** Histological scores based on analysis of synovial hyperplasia, inflammatory cell infiltration, bone destruction, and cartilage destruction. Mean ± s.e.m. ($n = 6$ per group, $^{*}p < 0.05$, $^{**}p < 0.01$, $^{****}p < 0.0001$). **H** COL2+ and ACAN+ chondrocytes were quantified. Mean ± s.e.m. ($n = 6$ per group, $^{****}p < 0.0001$). All error bars denote Mean ± s.e.m.; dots indicate individual samples/rats.

administrated with saline (Fig. 6F, G). These results suggest that SEMA3E could be a novel therapeutic potential for alleviating joint damage in RA patients. En-MSCs$^{C/I}$, through SEMA3E secretion, may provide a safer and more effective treatment for RA-related synovial inflammation and cartilage damage.

Discussion

Currently available drugs for treating RA lack selectivity and struggle to effectively moving to affected tissue, often resulting in undesirable side effects and toxicity[6,7,38]. There is an urgent need for a novel delivery system that can target therapeutic drugs precisely to the affected tissue to minimize side effects and improve therapeutic efficacy. Therefore, the main goal of the present study is to develop a biological delivery tool capable of specifically targeting RA-affected tissue for targeted therapy, while ensuring safety and controllability for clinical application. In this study, we employed En-MSCs$^{C/I}$ to effectively reduce inflammation in the synovial tissue of CIA rats, promote joints repair, and promote cartilage tissue regeneration. The absence of nuclei further minimizes the risks of long-term proliferation or

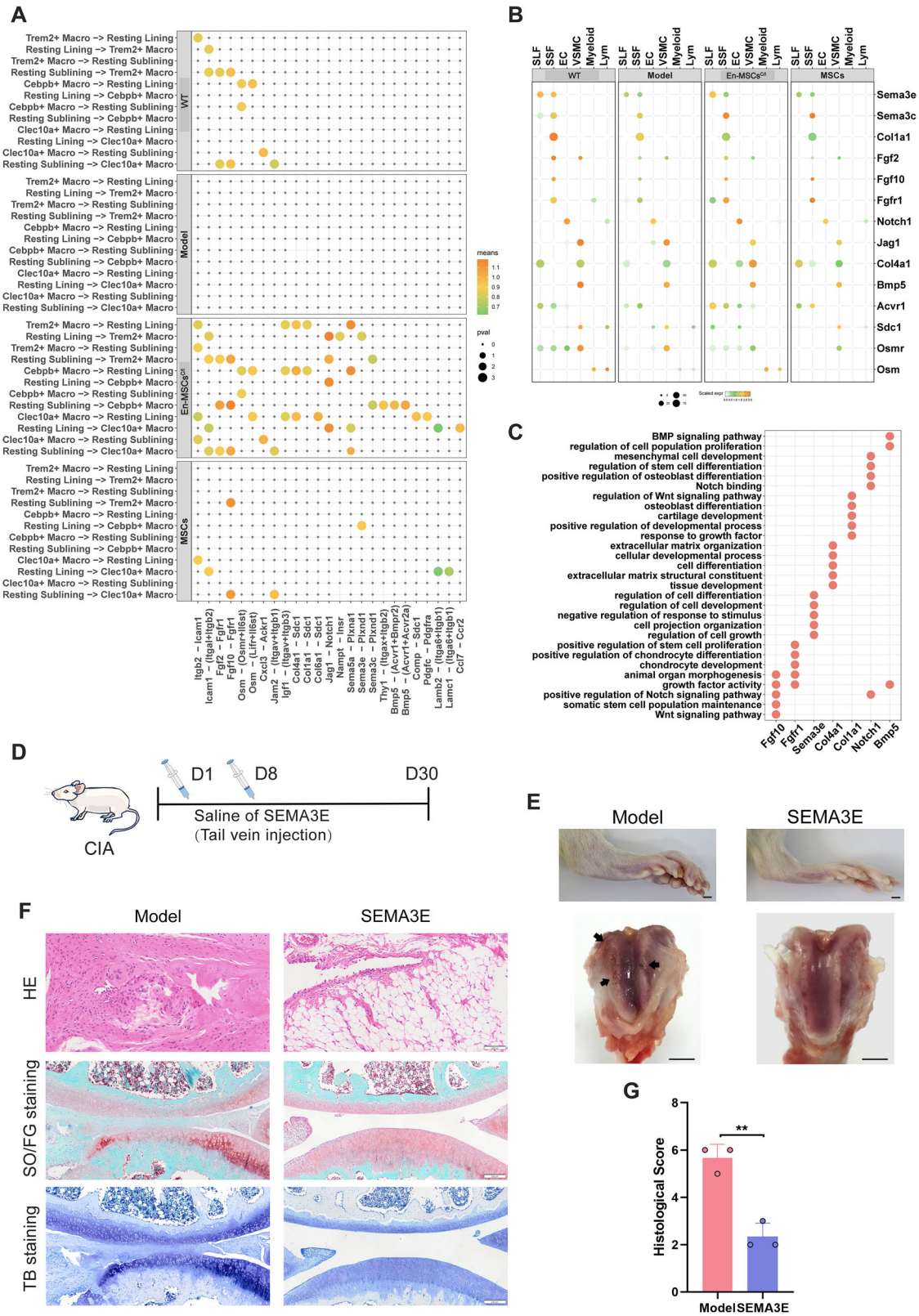

Fig. 6 | Administration of SEMA3E ameliorated synovial inflammation and cartilage damage in CIA rats. A Significant ligand-receptor pairs mediating signals between FLS clusters (resting lining and resting sublining) and STM clusters (Trem2+ macro, Cebpb+ macro and Clec10a+ macro). The dot color and size representing the calculated communication probability and *p*-value. *p*-value are computed from one-sided permutation test. **B** Dot plots showing gene expression levels and percentages for significant ligand-receptor pairs in each synovial cluster. **C** GO biological processes of genes in the significant ligand-receptor pairs shown in (**A**). **D** Experimental scheme for saline or SEMA3E treatment in CIA rat ($n = 3$). **E** Representative images from $n = 3$ biologically independent rat hind paws and knees after SEMA3E treatment for 4 weeks. Arrows indicated obvious cartilage damage and synovial hyperplasia in CIA rats treated with saline. Scale bar = 2 mm. **F** Representative histological images of cartilage treated with SEMA3E or saline per group. Joints were stained with H&E, safranin O, and toluidine blue, Scale bar = 200 μm. **G** Histological scores based on analysis of synovial hyperplasia, inflammatory cell infiltration, bone destruction, and cartilage destruction. ($n = 3$ per group, $^{**}p < 0.01$). All error bars denote Mean ± s.e.m.; dots indicate individual samples.

unwanted differentiation, thus enhancing their safety profile as a cell-free therapeutic platform.

The therapeutic potential of MSCs in RA treatment has been intensively studied in preclinical and clinical studies[39,40]. Typically, MSCs are administered intravenously, where they then migrate to the damaged area through interactions with selectins, integrins, chemokines and their receptors[41]. Nevertheless, numerous imaging studies reveal significant entrapment of MSCs within lung capillaries post-transplantation[42]. Cultivation and expansion of MSCs in vitro loss of key homing molecules, such as CXCR4, which diminished the opportunity of MSCs reaching target tissues[43]. Recently strategies, including gene modification, targeted delivery, and tissue modification have been explored to address these challenges[14]. However, gene modification raises safety concerns, and viral transduction is both time-consuming and costly. Other cell engineering methods are similarly intricate, requiring numerous reaction steps and optimization of individual ligands or receptors. We employed viral transfection method to induce the overexpression of CCR2 and IFN-γ in En-MSCs$^{C/I}$. The dual engineering of En-MSCs with CCR2 and IFN-γ represents a rational approach to simultaneously improve their homing efficiency and immunomodulatory potential. This strategy enables En-MSCs$^{C/I}$ to reach inflammatory sites more effectively and exert stronger local anti-inflammatory effects, even in the absence of nuclei. During the de-nuclearization process, integrated genome from the viral transfection was effectively eliminated, thereby mitigating significant safety concerns. Compared to MSCs, En-MSCs$^{C/I}$ exhibit reduced size post-de-nuclearization, resulting in a marked decrease in cell retention within the lungs and enhancing their homing efficiency to injured joint tissues. En-MSCs$^{C/I}$ exhibit an enhanced capacity to respond to specific inflammation-related chemokines within the affected joint tissue after entering the bloodstream. The marked upregulation of chemokine receptors on En-MSCs$^{C/I}$ significantly improved their therapeutic delivery to the damaged joint area. Notably, En-MSCs$^{C/I}$ have migrated to the injured hind limb knee joint for subsequent regulatory secretion within 24 h. Although En-MSCs$^{C/I}$ lack nuclei and are unable to proliferate, our in vitro and in vivo results suggest that they retain sufficient short-term viability to exert therapeutic effects. Trypan Blue exclusion assays showed that En-MSCs$^{C/I}$ remained viable for at least 72 h after enucleation, and in vivo bioluminescence imaging confirmed their homing and signal retention in inflamed joints for up to 72 h post-injection. However, the precise lifespan and clearance kinetics of En-MSCs$^{C/I}$ in vivo remain to be fully elucidated. Future studies employing long-term tracking methods will be important to better understand their biodistribution, degradation, and immunological fate. This information will be essential for optimizing dosage and administration frequency in clinical translation.

Interestingly, although MSCs and En-MSCs$^{C/I}$ exhibited different biodistribution patterns in vivo, both achieved therapeutic efficacy in reducing synovial inflammation and cartilage damage. This paradox may be explained by their distinct modes of action: MSCs may function primarily through systemic immunomodulation, including cytokine secretion and modulation of immune cells. In contrast, En-MSCs$^{C/I}$ exert localized effects by homing to the joint microenvironment, thereby amplifying local immunoregulatory functions. These findings suggest that both systemic and local immunoregulatory effects can independently alleviate RA pathology. However, further studies employing transcriptomic profiling and functional assays are necessary to precisely delineate these mechanistic differences.

A limitation of the current study is the absence of a direct comparison between MSCs overexpressing CCR2 and IFN-γ (MSCs$^{C/I}$) and En-MSCs$^{C/I}$. In this study, our goal was to develop En-MSCs$^{C/I}$ as a nucleus-free therapeutic approach designed to enhance safety and enhance therapeutic benefit. By eliminating the nucleus, this approach avoids the long-term risks of genomic integration, uncontrolled proliferation, or malignant transformation that may accompany intact MSCs, especially those genetically modified MSCs. At the same time, En-MSCs$^{C/I}$ retain desirable properties, including targeted homing and immunomodulatory functions, leading to efficacy comparable to conventional MSCs in our RA model. This nucleus-free, genetically enhanced strategy may thus offer a safer and more clinically translatable alternative to conventional MSC-based gene therapies.

The current understanding of RA is primarily driven by interactions among various cell types[44–46]. The heterogeneity of the multiple cell subpopulations at different stages of RA has been specifically elucidated and discussed. In healthy state, the synovium functions as a non-barrier immune quiescent tissue[47,48]. Following the onset of RA, the synovium undergoes significant activation and infiltration by innate and adaptive immune cells[28,49–51]. Activated immune cells produce cytokines and other mediators that act on the fibroblasts of the synovium, leading to the transformation of quiescent synovium cells into different subtypes and states[52–54].

ScRNA-seq in CIA rat models revealed synovial fibroblast alterations En-MSCs$^{C/I}$ and MSCs treatment. CIA rats exhibited expanded activated lining fibroblasts linked via GO analysis to immune/inflammatory processes and immune cell migration. While healthy synovial myeloid cells maintain homeostasis, monocytes/macrophages drive disease progression. MSC transplantation effects on synovial crosstalk remain undefined but may reveal critical therapeutic targets. Both En-MSCs$^{C/I}$ and MSCs similarly reduced synovial vascularization, attenuated inflammation, and modulated immune microenvironments by regulating activated lining/sublining fibroblasts and HBEGF + /CEBPB+ myeloid clusters, mitigating joint destruction. Fibroblast-myeloid interactions drove inflammatory aggregation and pro-inflammatory secretion, particularly activated lining-HBEGF+ monocyte crosstalk via ligands (Cxcl12, Csf, Hbegf, Spp1) promoting immune proliferation and joint deterioration. Both treatments disrupted this axis and attenuated macrophage polarization, restoring immune homeostasis.

En-MSCs$^{C/I}$ uniquely increased resting sublining cells expressing chondrogenic progenitor markers (CD34/Pi16/Mfap5). Multi-omics confirmed cartilage/bone development pathway enrichment, supported by superior in vitro chondrocyte repair and synovial medium-enhanced proliferation of damaged chondrocytes. En-MSCs$^{C/I}$ outperformed MSCs in cartilage repair, achieving near-complete joint restoration with elevated ACAN and COL2 approaching control levels, indicating hyaline-like regeneration via enhanced homing-activated secretion of regenerative factors.

En-MSCs$^{C/I}$ amplified fibroblast-myeloid crosstalk presents novel therapeutic potential. Prior studies link immunoregulatory semaphoring SEMA3E to angiogenesis suppression, macrophage repolarization, and tissue remodeling, supporting its joint-protective function[32,55,56]. While exogenous SEMA3E recapitulated cell therapy benefits, its molecular mechanisms remain uncharacterized. Future studies will focus on elucidating the pharmacokinetics, receptor interactions, and downstream pathways of SEMA3E in joint tissues. It will also be important to investigate how SEMA3E modulates immune cell recruitment, angiogenesis, and matrix remodeling in the arthritic microenvironment. These results will help clarify whether SEMA3E alone is sufficient as a therapeutic agent, or whether it functions best in the context of cell-based delivery. We acknowledge this as a limitation of the present study and propose SEMA3E signaling as a promising target for future mechanistic and translational exploration.

Materials and methods

Sex as a biological variable

Our study contained samples from male rats, because male animals exhibited less variability in phenotype. The physical condition of female rats is relatively inferior to that of male rats. They show lower tolerance to the establishment of type II collagen models and are more likely to have the experimental results interfered with by factors, such as estrogen or lifestyle habits[57,58].

Isolation and cultivation of MSCs

Human umbilical cords were collected from healthy donors who provided written informed consent prior to tissue donation. All procedures were conducted under protocols approved by the Ethics Committee of Yunnan

First People's Hospital (approval no. KHLL2018-GXB002). All ethical regulations relevant to human research participants were followed. Sex information of the umbilical cells was not provided by the supplier due to anonymization of tissue sources.

After removing the blood vessels, the umbilical cord was chopped and evenly distributed in 10 cm culture dishes. These dishes were then placed in an incubator at 37 °C until the tissue was adhered to the surface. Subsequently, MEM (25200056, Gibco, USA) medium containing 5% fetal bovine serum (F8318, Sigma-aldrich, USA) and 1% penicillin/streptomycin (15140122, Gibco, USA) was added. The medium was refreshed every other day, and MSCs growth around the tissues was monitored. Once MSCs grew all over the bottom of the culture dish, the tissues were removed, and the adherent cells were digested with 0.25% Trysin-EDTA (25200056, Gibco, USA) and collected by centrifugation for spare use. If necessary, the tissue can be cultured again following the same procedure.

Lentivirus transduction

Human MSCs were seeded in 24well plates, and sequentially infected with HBLV-IFNγ-3xflag-GFP and HBLV-CCR2-3xflag-GFP (HANBIO) at different multiplicities of infection (MOI) of 30, 50, 70, 100 PFU. The transfection efficiency was evaluated by measuring the proportion of GFP-positive MSCs under a fluorescence microscope. The MSCs and En-MSCs used for in vivo bioluminescence imaging were both transfected with HBLV-3xflag-GFP using viruses, GFP was co-expressed as part of the CCR2/IFN-γ lentiviral construct in En-MSCs$^{C/I}$.

Cell enucleation

Cell enucleation was adapted from the previously published protocol[18]. Briefly, Ficoll PM400 (Sigma, F4375) was dissolved in PBS to a 50% (wt/wt) solution by continual magnetic stirring for 24 h at room temperature, and then autoclaved. The Ficoll stock was aliquoted and stored at−20 °C. To prepare discontinuous gradients, the 50% Ficoll stock solution was diluted to 25% with MEM (HyClone, AJ30753334) and further diluted with MEM to prepare 17, 16, 15, and 12.5% Ficoll solutions. Cytochalasin B (Sigma Aldrich, 391163) was added to all Ficoll solutions at a final concentration of 10 μg/ml. Ficoll solutions (2 ml of 25%, 2 ml of 17%, 0.5 ml of 16%, 0.5 ml of 15% and 2 ml of 12.5%) were carefully layered into a 13.2 ml ultra-clear tube (Eppendorf, 345320 A) and equilibrated overnight in a 37 °C tissue culture incubator. MSCs were collected with trypsin (Gibco, 2868000), resuspended in 3.2 ml 12.5% Ficoll solution, and then carefully loaded onto the prepared discontinuous gradients, and topped with MEM. Tubes were balanced in swing buckets of the p65 rotor and centrifuged at 26,000 rpm for 60 minutes at 31 °C in a HIMAC CP100NX ultracentrifuge with minimal braking. Fractions were collected with MEM into centrifuge tubes and washed with PBS 3 times.

Diameters of enucleated MSCs were measured with the NIS-Elements AR 3.0 software (Nikon. AX/R). Enucleation efficiency was assessed using an epifluorescence microscope (Nikon AX/R) after staining with F-actin (Abcam, ab112125) for 30 min. Cellular internal morphology and organelles were visualized using a transmission electron microscopy (Hitachi, HT7800).

Assessment of enucleation and phenotype efficiency flow cytometry

To evaluate enucleation efficiency, cells were stained with 1 μg/mL DAPI (Sigma-Aldrich, USA) for 5 minutes at room temperature in the dark. Stained cells were analyzed using flow cytometry (BD FACSAria III). Viable cells were gated based on FSC/SSC characteristics, and the DAPI– population was quantified. Enucleation efficiency was defined as the percentage of DAPI-negative cells among total viable cells. Each experiment was performed in triplicate.

The immunophenotype of MSCs and En-MSCs$^{C/I}$ was evaluated by flow cytometry. Cells were collected, washed with PBS, and incubated with fluorochrome-conjugated antibodies against CD44, CD73 and CD90 (positive markers), as well as negative markers cocktail (CD45, CD34, CD11b, CD19 and HLA-DR) for 30 min at 4 °C in the dark. After washing, the cells were resuspended in PBS and analyzed using a flow cytometer (BD FACSCanto II). Data were processed with FlowJo software. Unstained cells and single-stained controls were used for compensation and gating.

Cell viability analysis

Cell viability of MSCs and En-MSCs$^{C/I}$ was assessed using the Trypan Blue exclusion method with an automated cell counter (Countstar). Cells were mixed 1:1 with 0.4% Trypan Blue (Gibco) and analyzed immediately. Viability was calculated as the percentage of unstained (live) cells out of the total cell population.

Western blot analysis

To evaluate the impact of enucleation on structural proteins, total proteins were extracted from MSCs and En-MSCs$^{C/I}$ using RIPA buffer containing protease inhibitors. After quantifying the protein concentration, equal amounts were separated by SDS-PAGE and transferred to PVDF membranes. The membranes were incubated with primary antibodies against LMNA/C, SUN2, Tubulin, Vimentin, FAK, β-actin, and GAPDH, followed by incubation with HRP-conjugated secondary antibodies. Protein bands were visualized using an ECL detection kit, and densitometric analysis was performed using ImageJ. GAPDH was used as the internal control for normalization. The following primary antibodies were used: Tubulin (Abcam, ab18207,1:2000), LMNA/C (ABclonal, AD249,1:1000), SUN2 (ABclonal, A16325,1:1000), Vimentin (ABclonal, A11952,1:1000), FAK (ABclonal, A11195,1:1000), β-actin (Abcam, ab179467,1:1000), GAPDH (affinity, AF7021,1:1000). Goat Anti-Rabbit IgG H&L (HRP) (Abcam, ab205718,1:2000).

Scratch wound healing assay

MSCs and En-MSCs$^{C/I}$ was seeded into 6-well plates and grown to 90% confluence. A uniform scratch was made through the cell monolayer using a 10 μL pipette tip. Floating cells were removed by washing with PBS, and serum-free medium was added. Images were captured at 0, 24, and 48 hours from the same field of view. The residual wound area was quantified using ImageJ software to assess cell migration ability.

Transwell chemotaxis assay

To evaluate the functionality of exogenously expressed CCR2, a CCL2-induced Transwell chemotaxis assay was performed. Twenty-four–well Transwell inserts (8 μm pore size, Corning) were used. MSCs, MSCs$^{C/I}$, En-MSCs and En-MSCs$^{C/I}$ was suspended in serum-free medium at a density of 1×10^5 cells in 100 μL and seeded into the upper chambers. The lower chambers were filled with 600 μL medium containing recombinant rat CCL2 (10 ng/mL, PeproTech). Cells were incubated for 6 or 12 h at 37 °C in a humidified atmosphere with 5% CO_2. At the end of incubation, non-migrated cells on the upper surface were gently removed with a cotton swab. Migrated cells on the underside of the membrane were fixed and stained with crystal violet. All experiments were repeated independently at least three times.

Induction and assessment of collagen-induced synovial inflammation in rat

Six to eight-week-old male Sprague-Dawley rats (SPF (Beijing) Biotechnology Co., Ltd., China., license No. SCXK [Beijing] 2024-0001) were used for all animal experiments. The rats are housed in the animal facility at Kunming University of Science and Technology, where all water and cages undergo sterilization. They are provided with granular feed according to a circadian rhythm. All animal procedures were approved by the Institutional Animal Care and Use Committee of Kunming University of Science and Technology (PZWHK2023-0002) and adhered to the Guide for the Care and Use of Laboratory Animals.We have complied with all relevant ethical regulations for animal use.

The CIA model was established in rats using type II collagen. Type II collagen (2 mg/mL) was mixed with complete Freund's adjuvant (CFA) in a 1:1 ratio. Rats were injected subcutaneously at multiple sites on their backs

with 0.15 ml/100 g of the inducing agent once a week for two weeks. Joint inflammation was monitored twice a week. The severity of arthritis was assessed based on paw pads edema and arthritis score: 0 = normal; 1 = mild edema and redness in the ankle joint; 2 = mild edema and redness in the ankle joint to the metacarpal or metacarpophalangeal joint; 3 = moderate edema and redness in the ankle joint to the metacarpal or metacarpophalangeal joint; 4 = severe edema and stiffness in the ankle joint with difficulty in movement. At four weeks post-induction, rats with arthritis scores of 3 or 4 were considered successfully modeled. In addition, A WT (wild-type) group of healthy *Sprague–Dawley* rats, without collagen induction or any treatment, was included as the normal control group.

En-MSCs$^{C/I}$ and MSCs transplantation in CIA rats

Following the four weeks post-administration of type II collagen, group allocation and coding were performed in a blinded manner by investigators not involved in the experiments. In addition to the WT control group, which comprised six rats without any immunization or intervention and served as healthy controls, CIA rats were randomly assigned to four experimental groups with six rats each. The CIA rats in the RA model group received 0.8 mL PBS through tail vein. The CIA rats in the En-MSCs groups were injected with 0.8 mL of enucleated MSCs without lentiviral transfection (5×10^6 cells/mL in PBS), the En-MSCs$^{C/I}$ groups were injected with 0.8 mL of enucleated MSCs$^{CCR2+/IFN\text{-}\gamma+}$($5 \times 10^6$ cells/mL in PBS), while the CIA rats in the MSCs groups were injected with 0.8 mL of MSCs (5×10^6 cells/mL in PBS). After transplantation, in vivo bioluminescence imaging was performed at 24, 48, and 72 h to track cell distribution. Arthritis scores and paw pad edema were assessed once weekly for six consecutive weeks, with evaluations performed in a blinded manner by independent observers. Serum was then collected for ELISA assays, followed by micro-CT scanning of the hind knee joints. After scanning, rats were euthanized by 5% isoflurane until loss of pedal reflex and cessation of respiration, with death confirmed by absence of heartbeat for >2 min. The hind knee joints were harvested for histopathological and immunohistochemical analyse.

Enzyme-linked immunosorbent assay (ELISA)

Blood samples were collected by cardiac puncture under 4% isoflurane anesthesia at the end of the experiment. Serum was separated by centrifugation (3000 rpm, 10 min, 4 °C) and stored at −80 °C for ELISA analysis. The levels of cytokines, including TNF-α, IL-1β, RF and CRP in serum samples were measured using commercial ELISA kits (R&D Systems) according to the manufacturer's instructions. Samples were analyzed in 96-well plates, and absorbance was read at 450 nm using a microplate reader. All assays were performed in triplicate, and standard curves were generated for quantification.

Micro-CT scanning

At 6 weeks post-transplantation, for micro-CT scanning, rats were anesthetized with 2% isoflurane and gently immobilized in a prone position on the specimen holder to minimize motion artifacts during imaging. Micro-CT scanning of the hind knee joints was performed using a Bruker SKYSCAN 1276 system. focusing on the sagittal plane of the tibial plateau to assess joint structural changes. Image data were reconstructed and quantitatively analyzed using Bruker's software package.

Histological evaluation

Arthritic tissue samples were harvested at six weeks post-transplantation. The tissues were fixed in 4% paraformaldehyde, embedded in paraffin, and sectioned at 7 μm thickness. The tissues sections were subjected to hematoxylin and eosin (H&E) staining, Safranin O-Fast Green and toluidine blue staining, and observed under an inverted microscope (Olympus, Japan).

Immunohistochemical and immunofluorescence staining and analysis

Synovial inflammation was visualized via immunostaining. The tissue sections were washed in PBS for 5 minutes at room temperature, treated with 3% methanol hydrogen peroxide, permeabilizated with 0.25% TritonX-100, and blocked with 10% goat serum for 1 hour. The primary antibodies were incubated overnight at 4 °C, and the information of the antibodies are listed as follows: INOS (ABCAM, ab283655, 1:2000), IL1β (ABCAM, ab283818, 1:400), TNF-α antibody (Thermo, PA1-40281, 1:50), COL2 (Thermo, PA5-99159, 1:100) and ACAN (Thermo, MA5-32695, 1:200). After being washed with PBS for 3 times, the sections were incubated with goat anti-rabbit IgG (Thermofisher, G-21234, 1:500) or goat anti-mouse IgG (Thermofisher, TI272496, 1:500) at room temperature for 2 hours. The immunohistochemical reaction was completed with Metal Enhanced DAB Substrate Kit (Thermofisher, TG267781), and then the image acquisition was procced with a microscope (OLYMPUS-BX-51). Inflammatory conditions across various experimental groups through HE staining. The grading system for inflammation was categorized as follows: 0 points (normal), 1 point (mild), 2 points (moderate), and 3 points (severe)[59]. The grading system of histological scores as categorized as follow: 0 (Normal), 0.5(Minimal degeneration), 1(Very mild degeneration), 2(Mild degeneration), 3(Moderate degeneration, 4(Marked degeneration), 5(Severe degeneration), 6(Very severe degeneration)[60].

For immunofluorescence staining, the following primary antibodies were used: CD74(SantaCruz,sc-6262,1:100), Prg4(ABCAM,28484,1:400),-TREM2 antibody (invitrogen, 3AABDA30, 1:150), CD68 antibody (invitrogen,2740420, 1:200), CXCL12 antibody (Santa Cruz,sc-74271, 1:50), HBEGF antibody (Santa Cruz,sc-365182, 1:150), CLEC10A antibody (Santa Cruz,sc-365182, 1:50), Ly6c antibody (ABCAM,ab318272, 1:100), CD68 antibody (ABCAM,ab283654, 1:200), CD34 antibody (ABCAM,ab81289, 1:50), COL2 antibody (ABCAM,ab34712, 1:300) and Ki67 (Abclonal,A16919, 1:200). The primary antibodies were incubated with the tissue's sections overnight at 4°C, followed by incubation with goat anti-mouse IgG coupled with Alexa Fluor 594 (Abcam, ab150116, 1:1000) and goat anti-rabbit antibody coupled with Alexa Fluor 647 (Thermofisher, TF266577, 1:500) for 2 hours at room temperature. Then, the fluorescent-stained sections were visualized using a confocal microscope (Lecia TCSSP8, XX) with excitation wavelengths at 405, 488, 594 and 647 nm.

In vivo bioluminescence imaging (BLI)

To assess the homing and persistence of transplanted cells, a random subset of CIA rats ($n = 3$ per group) was selected for BLI. CIA rats were intravenously injected with GFP-labeled MSCs, En-MSCs or En-MSCs$^{C/I}$. Fluorescence imaging was performed at 24, 48, and 72 h post-injection using the IVIS Spectrum imaging system (PerkinElmer, USA). Total photon flux within the region of interest (ROI) around the joints was quantified using Living Image software.

Single-cell RNA-seq data processing

Articular cartilage tissues were harvested from the knee joints of CIA rats at the experimental endpoint. Samples were immediately transferred into cold PBS and minced into ~1 mm^3 fragments. The tissue was digested with 4 mg/mL collagenase (Sigma, V900892) at 37 °C with gentle agitation for 4–6 h. The digested suspension was then filtered sequentially through 70 and 40 μm strainers (Corning, USA) to remove undigested debris, followed by centrifugation at 300 × g for 5 min. The resulting cell pellet was resuspended in PBS containing 0.04% BSA. Cell viability (> 90%) was confirmed using trypan blue exclusion, and concentration of the single-cell suspension was adjusted to 1000–1200 cells/μl for library construction using the 10x Genomics Chromium Single Cell 3′ v3.1 platform.

FASTQ reads of the 10x scRNA-seq data were processed for barcode and UMI counting with mRatBN7 reference genome using Cell Ranger (version 3.1, 10x Genomics). After consolidating the various sets of processing matrices, we employed Seurat (version 4.2.0) for subsequent statistical analysis. The quality control of scRNA-seq data involved the application of multiple filtering parameters, including the requirement for a gene count between 200 and 6,000 and a mitochondrial RNA content of less than 20%. The filtered data was subsequently processed using DoubletFinder (version 2.0.3) to mitigate the impact of multiplets. The preprocessed expression matrix was normalized and log2-transformed.

Perform principal component analysis (PCA) on the scaled data of all cells using the top 2000 highly variable genes and retain the top 20 principal components (PCs). performed Batch correction was performed using Harmony (version 0.1.1) based on the PCs described above. Using Seurat's FindNeighbors and FindClusters functions to group cells into the optimal number of clusters can enhance the subsequent cell type annotation. Finally, a total of 103,406 cells extracted from complete synovial tissues were used for downstream analysis.

We used differentially expressed genes (DGE) (p-value < 0.05 and log FC > 0.25) for the identification of specific cell types. All reported p-value underwent adjustment using the Bonferroni correction. To help annotate the subpopulations in each cell region, we used the Wilcoxon rank sum test in the Seurat workflow to calculate the DEGs. Through a combined analysis of the results from the FindAllMarkers function for DGE analysis and reference to known phenotypic markers, we identified marker genes for each cell cluster, as detailed in Supplementary Data 1. We identified 6 clusters: EC, VSMC, SLF, SSF, myeloid cells (Myeloid), and Lym.

Gene set score

We used the AddMouduleScore function in Seurat to calculate the enrichment of genes involved in macrophage polarization (the number of control features selected from the same partition for each analyzed feature is 100). A list of genes was collected upon literature research[50,61,62] (Supplementary Data 2). Mann-Whitney U test was performed for comparison between two groups.

Identifying enriched gene pathways

To further elucidate the functions of distinct cell subtypes, the enriched gene pathways were identified using pre-ranked GSEA by FGSEA (version 1.28.0). To assess the pathway enrichment of different experimental groups for the same cell subpopulation, we used KEGG subsets by clusterProfiler (version 4.10.1) We considered that the path with a Benjamini-Hochberg corrected p-value of less than 0.05 is statistically significant. All the enriched pathways mentioned in the paper all among the top 100.

Pseudotime trajectory inference

We used Monocle3 (version 1.3.4) to generate pseudo-time trajectories to measure the differentiation process of fibroblasts based on single-cell data profiles from different experimental groups. Data preprocessing involved the same dimensionality reduction techniques used in Seurat-based analyses, with UMAP used for nonlinear dimensionality reduction. After trajectories were reconstructed by the learn_graph function, the cells are ordered in pseudotime using the order cellsfunction. The location of the Mfap5+ Dpp4+ cluster identifies a node which as the initial node of the pseudotime trajectory.

Cell-cell communication analysis

CellChat (version 1.6.1) was used to infer potential signaling pathways and interactions among distinct clusters. We cross-analyzed various fibroblast cells and myeloid cells, focusing on the primary cell group signaling. Various modes of cellular interaction (Secreted Signaling, ECM-Receptor, Cell-Cell Contact) have been predicted in order to gain a comprehensive understanding of intercellular interactions. Over-expressed genes and ligand-receptor interactions were identified with default identifyOverExpressedGenes and identifyOverExpressedInteractions functions. The computeCommunProb function was used to determine the communication probability associated with all ligand-receptor interactions for each signaling pathway, thereby inferring biologically significant cell-cell communication. Cellular pathways with fewer than 10 cells involved were removed. To ensure the relevance and accuracy of the analysis, only ligand-receptor pairs with a p-value less than 0.05 were considered.

Gene expression analysis by qRT-PCR

For the in vivo validation, synovial tissues were harvested from a random subset of CIA rats ($n = 4$) following transplantation. Total RNA from all samples of differents group was extracted using Trizol® reagent (Thermo Fisher Scientific, USA). The collected RNA was dissolved in sterile diethyl pyrocarbonate-treated water (Sangon Biotech, China), and cDNA was synthesized using a PrimeScript RT reagent kit (Takara, Japan) at 37 °C for 5 min and 85 °C for 5 s. Quantification of specific genes was performed using SYBR® Premix Ex TaqTM II kit (Takara, Japan) and CXF real-time PCR system (Bio-Rad Laboratories, USA) under the following conditions: Stage 1: 95 °C for 3 s; Stage 2: 95 °C for 3 s; 60 °C for 30 s, and repeat for 37 cycles. All experiments were performed in triplicate, and data were analyzed using the $2^{-\Delta\Delta Ct}$ method. For the in vitro assays, primary synovial cells and chondrocytes were isolated after treatment with different cell types, and the subsequent procedures were the same as described above. All the primers were commercially synthesized (Sangon Biotech, China), and the primers' sequences are listed below:

IGF1: CACATCTCTTCTACCTGGCA GGTCCACACACGAACT GAA

GAS6: CGACTACCACTCCACAAAGAA GCACACCTTGATTTC CATC

FGF: TCCAAGCAGAAGAGAGAGGA CACACTTAGAAGCCAG CAGC

COMP: AACTGGGTGGTGCTCAAT CAGCGTAGTCATCATC GGT

SOX5: AAATGACCACGATGCTGTC ATACCTATGCTGTTCAC TACGG

SOX9: TGAGTTTGACCAATACCTGC CCTGTTGCTTTGACA TCCA

TGFB2: CACTTTCTACAGACCCTACTTCAG CTGCCTTCACC AGATTTGA

ACAN: CCTGGACAAGTGCTATGCT GGTAGAGGTAGACAGT TCTCACG

COL2: CCAGAACATCACCTACCACTGT CCCTCATCTCCACAT CATTG

MMP13: TTTGGCTTAGATGTGACTGG TGGGACCATTTGAG TGTTC

TGFβ3: CACATCAAGAAGAAGAGGGTG GTTGTAAAGTGCC AGGACCT

COL9: TTGTGTCCCAATGCCTGT CACCCTTGTGTCCTTGT CTT

IL-1β: CCTGTTCTTTGAGGCTGACA CGAGATGCTGCTGTG AGAT

TNF-α: GCCTCAGCCTCTTCTCATT TTCTCCTCCTTGTTGG GAC

CXCL12: CCTGCCGATTCTTTGAGA GCACACTTGTCTGTTG TTGC

CCL2: ACTCATTCACTGGCAAGATG TGGACCCATTCCTTA TTGG

MMP1: ATTCTGAAACCCTGAGTGCT TGGTCCAACGAGGA TTGT

Induction and assessment of collagen-induced cartilage damage in rats

In line with the previous approach, we selected 6–8-week-old SD rats and induced the CIA model through subcutaneous injection of type II collagen and complete Freund's adjuvant. Type II collagen (2 mg/mL) was emulsified 1:1 with complete Freund's adjuvant and injected subcutaneously at multiple dorsal sites (0.15 mL/100 g) once a week for two consecutive weeks (day 0 and day 7) to induce CIA. The progression of synovial inflammation and cartilage damage was blindly evaluated based on joint mobility and arthritis scores(scores = 4), and was further confirmed by histopathological examination using HE staining and immunohistochemistry of joint sections at week 8 post-induction. Rats showing evident synovial invasion and cartilage damage were randomly divided into two groups ($n = 6$ per group) and injected with either En-MSCs$^{C/I}$ or MSCs via the tail vein. Six weeks after transplantation, joint damage in the hind limbs was evaluated. The joints underwent decalcification, paraffin embedding,

and subsequent sectioning for Saffron solid green, TB, COL2, and ACAN immunohistochemical staining.

Extraction and analysis of synovial and chondrocyte cells in vitro

At the end of the experiment, rats were euthanized by 5% isoflurane until loss of pedal reflex and cessation of respiration, with death confirmed by absence of heartbeat for >2 min. Under aseptic conditions, rats were discarding fat and fibrous tissues, synovium were dissected from the knee, cartilage tissues on the femoral condyle of the rat knee joint were separated. All the tissues washed twice with PBS, and cut into small pieces. Added 0.4% collagenase and digested the tissue further under a constant temperature in a shaker for 4-6 hours. Subsequently, we resuspended the digested cells and isolated synoviocyte and chondrocyte were seeded into 6-well plates or 24-well plates. Synoviocyte sub-cultured in MEM medium, chondrocyte sub-cultured in F12 medium, containing 10% fetal bovine serum, 100 U/mL penicillin and streptomycin, in an incubator at 37 °C with 5% CO_2. The cells were subsequently passaged every 3 days and P4 were used for further experiments.

Transwell assay

In vitro validation test of synoviocyte and chondrocyte was measured in a Transwell cell culture chamber apparatus with 3 μm pore membrane (Costar, 0522206, USA). Briefly, primary synoviocyte were seed at a density of 10^5 cell/well in 6-well plates, 10^4 cells/well in 24 well plates, and LPS (15 ng/ml) stimulated synoviocyte 24 h, Then, En-MSCs$^{C/I}$ and MSCs (5×10^4 cell/well) was loaded into the upper chamber of the Transwell insert. CXCR4 receptor agonist was added to the lower compartment α-MEM Medium. After 24 h of incubation, the filters were removed and synoviocyte in 24 well plates were fixed in 4% paraformaldehyde and then immunofluorescence stained with iNOS.

Primary chondrocyte was seeded at a density of 10^5 cell/well in 6-well plates, 10^4 cell/well in 24-well plates with F12 culture medium, and stimulated with H_2O_2 (400 ng/ml) for 24 h. Then En-MSCs$^{C/I}$ and MSCs (5×10^4 cell/well) was loaded into the upper chamber of the Transwell insert. synoviocytee medium was replaced to the lower compartment F12 culture medium. After 24 h of incubation, the filters were removed and chondrocyte in 24 well plates were fixed in 4% paraformaldehyde and then immunofluorescence stained with Ki67 and COL2. Chondrocyte in 6 well plates were extraction of total RNA.

SEMA3E administration in CIA rats

A recombinant SEMA3E treatment experiment was performed in CIA rats. At the start of the intervention, rats were randomly divided into two groups ($n = 3$ per group). One group received intra-articular injections of recombinant SEMA3E protein (Abbexa, abx069024) into the knee joint cavity at a dose of 50 μg/kg, administered once weekly during the first and second weeks (two doses in total). The control group received an equal volume of sterile saline. Four weeks after the first injection, rats were euthanized by 5% isoflurane until loss of pedal reflex and cessation of respiration, with death confirmed by absence of heartbeat for >2 min. Joint tissues were collected for histological and immunohistochemical evaluation of synovial inflammation and cartilage integrity.

Statistics and reproducibility

GraphPad Prism8 was used to analyze the data and determine statistical significance of differences between groups by applying Student's t-test, one-way or two-way analysis of variance (ANOVA) with post-hoc multiple comparisons test as indicated. Adjusted p-values < 0.05 were considered significant. Data are presented as Mean ± s.e.m unless otherwise stated.

All experiments were independently repeated at least three times. The exact n values and definitions of biological replicates are indicated in the corresponding figure legends. Technical replicates were averaged within each biological replicate and not treated as independent samples. Randomization and blinding were applied for animal allocation, arthritis scoring, and histological evaluations.

Data availability

All uncropped and unprocessed full-scan blots and gels underlying the figures are provided in the Supplementary Information; The sequencing data generated in this study have been deposited in the National Genomics Data Center (NGDC) under accession number CRA019929 (https://ngdc.cncb.ac.cn). Source data underlying the single cell RNA-Seq graphs and charts presented in the main Figures are provided in the Supplementary Data 1 and Supplementary Data 2. All other data supporting the findings of this study are available from the corresponding author upon reasonable request.

Received: 16 April 2025; Accepted: 13 November 2025;
Published online: 27 November 2025

References

1. Safiri, S. et al. Global, regional and national burden of rheumatoid arthritis 1990-2017: a systematic analysis of the Global Burden of Disease study 2017. *Ann. Rheum. Dis.* **78**, 1463–1471 (2019).
2. Smolen, J. S., Aletaha, D. & McInnes, I. B. Rheumatoid arthritis. *Lancet* **388**, 2023–2038 (2016).
3. McInnes, I. B. & Schett, G. The pathogenesis of rheumatoid arthritis. *N. Engl. J. Med.* **365**, 2205–2219 (2011).
4. Singh, J. A. et al. 2015 American College of Rheumatology Guideline for the Treatment of Rheumatoid Arthritis. *Arthritis Rheumatol.* **68**, 1–26 (2016).
5. Smolen, J. S. et al. EULAR recommendations for the management of rheumatoid arthritis with synthetic and biological disease-modifying antirheumatic drugs. *Ann. Rheum. Dis.* **69**, 964–975 (2010).
6. Baharlou, R. et al. Human adipose tissue-derived mesenchymal stem cells in rheumatoid arthritis: Regulatory effects on peripheral blood mononuclear cells activation. *Int. Immunopharmacol.* **47**, 59–69 (2017).
7. Shadmanfar, S. et al. Intra-articular knee implantation of autologous bone marrow-derived mesenchymal stromal cells in rheumatoid arthritis patients with knee involvement: Results of a randomized, triple-blind, placebo-controlled phase 1/2 clinical trial. *Cytotherapy* **20**, 499–506 (2018).
8. Thanuja, M. Y., Anupama, C. & Ranganath, S. H. Bioengineered cellular and cell membrane-derived vehicles for actively targeted drug delivery: So near and yet so far. *Adv. drug Deliv. Rev.* **132**, 57–80 (2018).
9. Labusca, L., Herea, D. D. & Mashayekhi, K. Stem cells as delivery vehicles for regenerative medicine-challenges and perspectives. *World J. Stem Cells* **10**, 43–56 (2018).
10. Le Blanc, K. & Mougiakakos, D. Multipotent mesenchymal stromal cells and the innate immune system. *Nat. Rev. Immunol.* **12**, 383–396 (2012).
11. Spees, J. L., Lee, R. H. & Gregory, C. A. Mechanisms of mesenchymal stem/stromal cell function. *Stem Cell Res. Ther.* **7**, 125 (2016).
12. Bertolino, G. M., Maumus, M., Jorgensen, C. & Noël, D. Therapeutic potential in rheumatic diseases of extracellular vesicles derived from mesenchymal stromal cells. *Nat. Rev. Rheumatol.* **19**, 682–694 (2023).
13. Boltze, J. et al. The dark side of the force - constraints and complications of cell therapies for stroke. *Front. Neurol.* **6**, 155 (2015).
14. Ullah, M., Liu, D. D. & Thakor, A. S. Mesenchymal stromal cell homing: mechanisms and strategies for improvement. *iScience* **15**, 421–438 (2019).
15. Fischer, U. M. et al. Pulmonary passage is a major obstacle for intravenous stem cell delivery: the pulmonary first-pass effect. *Stem Cells Dev.* **18**, 683–692 (2009).
16. Karp, J. M. & Leng Teo, G. S. Mesenchymal stem cell homing: the devil is in the details. *Cell Stem Cell* **4**, 206–216 (2009).
17. Galipeau, J. & Sensébé, L. Mesenchymal stromal cells: clinical challenges and therapeutic opportunities. *Cell Stem Cell* **22**, 824–833 (2018).

18. Wang, H. et al. Genetically engineered and enucleated human mesenchymal stromal cells for the targeted delivery of therapeutics to diseased tissue. *Nat. Biomed. Eng.* **6**, 882–897 (2022).
19. Cao, W., Cao, K., Cao, J., Wang, Y. & Shi, Y. Mesenchymal stem cells and adaptive immune responses. *Immunol. Lett.* **168**, 147–153 (2015).
20. Marks, P. W., Witten, C. M. & Califf, R. M. Clarifying stem-cell therapy's benefits and risks. *N. Engl. J. Med.* **376**, 1007–1009 (2017).
21. Ren, G. et al. Mesenchymal stem cell-mediated immunosuppression occurs via concerted action of chemokines and nitric oxide. *Cell Stem Cell* **2**, 141–150 (2008).
22. Cannon, G. W. et al. Double-blind trial of recombinant gamma-interferon versus placebo in the treatment of rheumatoid arthritis. *Arthritis Rheumatism* **32**, 964–973 (1989).
23. Samanta, S. et al. Exosomes: new molecular targets of diseases. *Acta Pharmacologica Sin.* **39**, 501–513 (2018).
24. Fang, R. H., Kroll, A. V., Gao, W. & Zhang, L. Cell membrane coating nanotechnology. *Adv. Mater.* **30**, e1706759 (2018).
25. Thomas, R. et al. Exogenous Semaphorin 3E treatment protects against chlamydial lung infection in mice. *Front. Immunol.* **13**, 882412 (2022).
26. Smith, M. H. et al. Drivers of heterogeneity in synovial fibroblasts in rheumatoid arthritis. *Nat. Immunol.* **24**, 1200–1210 (2023).
27. Nygaard, G. & Firestein, G. S. Restoring synovial homeostasis in rheumatoid arthritis by targeting fibroblast-like synoviocytes. *Nat. Rev. Rheumatol.* **16**, 316–333 (2020).
28. Culemann, S. et al. Locally renewing resident synovial macrophages provide a protective barrier for the joint. *Nature* **572**, 670–675 (2019).
29. Kuo, D. et al. HBEGF(+) macrophages in rheumatoid arthritis induce fibroblast invasiveness. *Sci. Transl. Med.* **11**, eaau8587 (2019).
30. Alivernini, S. et al. Distinct synovial tissue macrophage subsets regulate inflammation and remission in rheumatoid arthritis. *Nat. Med.* **26**, 1295–1306 (2020).
31. Micheroli, R. et al. Role of synovial fibroblast subsets across synovial pathotypes in rheumatoid arthritis: a deconvolution analysis. *RMD Open* **8**, e001949 (2022).
32. Serini, G. et al. Class 3 semaphorins control vascular morphogenesis by inhibiting integrin function. *Nature* **424**, 391–397 (2003).
33. Noueihed, B. et al. Mesenchymal stromal cells promote retinal vascular repair by modulating sema3E and IL-17A in a model of ischemic retinopathy. *Front. Cell Develop. Biol.* **9**, 630645 (2021).
34. Rosloniec, E. F., Cremer, M., Kang, A. & Myers, L. K. Collagen-induced arthritis. *Curr. Protoc. Immunol.* **15**, 15.15.11–15.15.24 (2001).
35. Griffiths, M. M. Immunogenetics of collagen-induced arthritis in rats. *Int. Rev. Immunol.* **4**, 1–15 (1988).
36. Knights, A. J. et al. Synovial fibroblasts assume distinct functional identities and secrete R-spondin 2 in osteoarthritis. *Ann. Rheum. Dis.* **82**, 272–282 (2023).
37. Thomas, R. et al. Semaphorin 3E protects against chlamydial infection by modulating dendritic cell functions. *J. Immunol.* **206**, 1251–1265 (2021).
38. Park, E. H. et al. Intravenous infusion of umbilical cord blood-derived mesenchymal stem cells in rheumatoid arthritis: a phase IA clinical trial. *Stem Cells Transl. Med.* **7**, 636–642 (2018).
39. Liu, L. et al. Meta-analysis of preclinical studies of mesenchymal stromal cells to treat rheumatoid arthritis. *EBioMedicine* **47**, 563–577 (2019).
40. Beeravolu, N. et al. Isolation and characterization of mesenchymal stromal cells from human umbilical cord and fetal placenta. *J. Vis. Exp.* **3**, 55224 (2017).
41. Sackstein, R. The lymphocyte homing receptors: gatekeepers of the multistep paradigm. *Curr. Opin. Hematol.* **12**, 444–450 (2005).
42. Scarfe, L. et al. Non-invasive imaging reveals conditions that impact distribution and persistence of cells after in vivo administration. *Stem Cell Res. Ther.* **9**, 332 (2018).
43. Von Lüttichau, I. et al. Human adult CD34- progenitor cells functionally express the chemokine receptors CCR1, CCR4, CCR7, CXCR5, and CCR10 but not CXCR4. *Stem cells Dev.* **14**, 329–336 (2005).
44. Guo, S. et al. Genome-wide DNA methylation patterns in CD4+ T cells from Chinese Han patients with rheumatoid arthritis. *Mod. Rheumatol.* **27**, 441–447 (2017).
45. Plant, D., Wilson, A. G. & Barton, A. Genetic and epigenetic predictors of responsiveness to treatment in RA. *Nat. Rev. Rheumatol.* **10**, 329–337 (2014).
46. Shi, Y. et al. Immunoregulatory mechanisms of mesenchymal stem and stromal cells in inflammatory diseases. *Nat. Rev. Nephrol.* **14**, 493–507 (2018).
47. Kurowska-Stolarska, M. & Alivernini, S. Synovial tissue macrophages in joint homeostasis, rheumatoid arthritis and disease remission. *Nat. Rev. Rheumatol.* **18**, 384–397 (2022).
48. Huang, Q. Q. et al. Critical role of synovial tissue-resident macrophage niche in joint homeostasis and suppression of chronic inflammation. *Sci. Adv.* **7**, eabd0515 (2021).
49. Mulder, K. et al. Cross-tissue single-cell landscape of human monocytes and macrophages in health and disease. *Immunity* **54**, 1883–1900 (2021).
50. Zhang, F. et al. Defining inflammatory cell states in rheumatoid arthritis joint synovial tissues by integrating single-cell transcriptomics and mass cytometry. *Nat. Immunol.* **20**, 928–942 (2019).
51. Takeuchi, Y., Hirota, K. & Sakaguchi, S. Synovial tissue inflammation mediated by autoimmune T cells. *Front. Immunol.* **10**, 1989 (2019).
52. Boots, A. M., Wimmers-Bertens, A. J. & Rijnders, A. W. Antigen-presenting capacity of rheumatoid synovial fibroblasts. *Immunology* **82**, 268–274 (1994).
53. Tran, C. N. et al. Presentation of arthritogenic peptide to antigen-specific T cells by fibroblast-like synoviocytes. *Arthritis Rheumatism* **56**, 1497–1506 (2007).
54. Carmona-Rivera, C. et al. Synovial fibroblast-neutrophil interactions promote pathogenic adaptive immunity in rheumatoid arthritis. *Sci. Immunol.* **2**, eaag3358 (2017).
55. Pecho-Vrieseling, E., Sigrist, M., Yoshida, Y., Jessell, T. M. & Arber, S. Specificity of sensory-motor connections encoded by Sema3e-Plxnd1 recognition. *Nature* **459**, 842–846 (2009).
56. Shimizu, I. et al. Semaphorin3E-induced inflammation contributes to insulin resistance in dietary obesity. *Cell Metab.* **18**, 491–504 (2013).
57. Dimitrijević, M. et al. Sex differences in Tfh cell help to B cells contribute to sexual dimorphism in severity of rat collagen-induced arthritis. *Sci. Rep.* **10**, 1214 (2020).
58. Dimitrijević, M. et al. Sex-based differences in monocytic lineage cells contribute to more severe collagen-induced arthritis in female rats compared with male rats. *Inflammation* **43**, 2312–2331 (2020).
59. Krenn, V. et al. Synovitis score: discrimination between chronic low-grade and high-grade synovitis. *Histopathology* **49**, 358–364 (2006).
60. Pritzker, K. P. et al. Osteoarthritis cartilage histopathology: grading and staging. *Osteoarthr. Cartil.* **14**, 13–29 (2006).
61. Liu, C. et al. Radioimmunotherapy-induced intratumoral changes in cervical squamous cell carcinoma at single-cell resolution. *Cancer Commun.* **42**, 1407–1411 (2022).
62. Ruan, Z. et al. Single-cell RNA sequencing unveils Lrg1's role in cerebral ischemia–reperfusion injury by modulating various cells. *J. Neuroinflamm.* **20**, 285 (2023).

Acknowledgements

This study was supported by grants from the National Natural Science Foundation of China of U23A20491; The Natural Science Foundation of Yunnan Province of 202202AG050018; The Yunnan Provincial Central Guided for Local Science and Technology Development Funds Project (202507AB040007). Special thanks are due to the instrumental/data analysis from Advanced Imaging Platform of Institute of Primate Translational Medicine, Kunming University of Science and Technology.

Author contributions

Y.S., Y.Y., Y.S., Y.L., Q.Q. and L.T. conducted biological experiments and data collection. W.S., Y.Y., N.Y., and Z.P. performed transcriptomic analysis. W.S., Y.Y., and Y.S. conceived and designed the experiments and analyses. W.S., and Y.S. prepared the paper. W.S. Y.S., and Y.Y. supervised the work.

Competing interests

The authors declare no competing interests.

Additional information

Supplementary information The online version contains supplementary material available at https://doi.org/10.1038/s42003-025-09248-5.

Correspondence and requests for materials should be addressed to Yaping Yan or Wei Si.

Peer review information *Communications Biology* thanks Wei Wang and the other, anonymous, reviewers for their contribution to the peer review of this work. Primary Handling Editor: Ophelia Bu.